International Journal of Extreme Manufacturing

Laser metal deposition of refractory high-entropy alloys for high-throughput synthesis and structure-property characterization

OPEN ACCESS
IOP Publishing | IMMT
International Journal of Extreme Manufacturing
Int. J. Extrem. Manuf. **3** (2021) 015201 (23pp)
https://doi.org/10.1088/2631-7990/abcca8

Laser metal deposition of refractory high-entropy alloys for high-throughput synthesis and structure-property characterization

Henrik Dobbelstein[1], Easo P George[2,3], Evgeny L Gurevich[1], Aleksander Kostka[4], Andreas Ostendorf[1] and Guillaume Laplanche[5]

[1] Applied Laser Technologies, Ruhr-University Bochum, Universitätsstr. 150, 44801 Bochum, Germany
[2] Material Science and Technology Division, Oak Ridge National Laboratory, Oak Ridge, TN 37831-6115, United States of America
[3] Materials Science and Engineering Department, University of Tennessee, Knoxville, TN 37996-2100, United States of America
[4] Center for Interface-Dominated High Performance Materials, Ruhr-University Bochum, Universitätsstr. 150, 44801 Bochum, Germany
[5] Institute for Materials, Ruhr-University Bochum, Universitätsstr. 150, 44801 Bochum, Germany

E-mail: dobbelstein@lat.rub.de

Received 18 June 2020, revised 18 October 2020
Accepted for publication 20 November 2020
Published 30 December 2020

Abstract

Progress in materials development is often paced by the time required to produce and evaluate a large number of alloys with different chemical compositions. This applies especially to refractory high-entropy alloys (RHEAs), which are difficult to synthesize and process by conventional methods. To evaluate a possible way to accelerate the process, high-throughput laser metal deposition was used in this work to prepare a quinary RHEA, TiZrNbHfTa, as well as its quaternary and ternary subsystems by *in-situ* alloying of elemental powders. Compositionally graded variants of the quinary RHEA were also analyzed. Our results show that the influence of various parameters such as powder shape and purity, alloy composition, and especially the solidification range, on the processability, microstructure, porosity, and mechanical properties can be investigated rapidly. The strength of these alloys was mainly affected by the oxygen and nitrogen contents of the starting powders, while substitutional solid solution strengthening played a minor role.

Keywords: high-entropy alloy, HfNbTaTiZr, refractory, powder blend, laser metal deposition, additive manufacturing, high-throughput synthesis

(Some figures may appear in colour only in the online journal)

1. Introduction

As discussed in recent review papers, high-entropy alloys (HEAs) (e.g. [1, 2],) and high-entropy ceramics (HECs) (e.g. [3, 4],) open vast compositional regions in which novel materials with interesting structural and functional properties may be discovered. However, this potential comes with the challenge of effectively producing and screening

these alloys. Conventional approaches based on casting, simulation, and experimental characterization are too time-consuming to cover such a large compositional space. Here we focus on an additive manufacturing technique, namely, laser metal deposition (LMD), to perform combinatorial high-throughput synthesis on a prototypical refractory high-entropy alloy (RHEA), titanium-zirconium-niobium-hafnium-tantalum (TiZrNbHfTa), and its lower-order subsystems. To investigate a broad range of compositions in the Ti-Zr-Nb-Hf-Ta system, compositional gradients were created and their microstructures and mechanical properties were screened. Since LMD depends on the availability and quality of raw powders, we also investigated how the particle size, shape, and purity of the powders affect processability and the resulting microstructures and mechanical properties. In the future, LMD might be used to fabricate more complex RHEA parts if the factors affecting the LMD process are sufficiently understood and controlled. To this end, additional equiatomic subsystems of the TiZrNbHfTa RHEA were produced by LMD. Finally, the various factors (e.g. quality of the built specimens, their microstructures, and alloy chemistry including interstitials) affecting the strength of the additively manufactured RHEAs were investigated in detail.

2. Background on refractory HEAs and their processability by additive manufacturing

2.1. Refractory HEAs

Senkov *et al* synthesized the first refractory single-phase body-centered cubic (bcc) HEAs, NbMoTaW and VNbMoTaW which [5, 6] were reported to have high yield strengths at elevated temperatures but ductility only in compression at room temperature. In contrast, the equiatomic TiZrNbHfTa alloy is both malleable and ductile in tension at room temperature [7]. Various groups have studied its microstructure [8], compressive properties at room and high temperature [6, 9–11], tensile properties [7, 12], elastic properties [13, 14], phase stability [15–18] and Ti/Zr/Hf-rich [19, 20] and Nb/Ta-rich [21] variations . Recently, Lei *et al* [22] reported that oxygen and nitrogen interstitials significantly influence the mechanical properties of the medium-entropy subsystem TiZrHfNb. This study shows that a similar effect can be expected in the TiZrNbHfTa. However, current literature rarely measures or reports oxygen and nitrogen concentrations.

2.2. High-throughput combinatorial synthesis of RHEAs and laser-based additive manufacturing

Additive manufacturing techniques, especially selective laser melting (SLM) and LMD, can be utilized to combinatorially synthesize high-melting-point RHEAs. Eventually these techniques may also find application in manufacturing complex 3D parts made from RHEAs. In both SLM and LMD, a pre-alloyed powder or a blend of different powders is locally melted with a focused laser beam that moves along a predefined path. SLM typically uses a pre-alloyed powder, and the workpiece resides in a powder bed. For this reason, SLM is less suitable than LMD for high-throughput compositional screening of HEAs. However, process parameters can be altered and the resulting microstructures and mechanical properties can be examined. Recent SLM studies focus primarily on HEAs that are available as pre-alloyed powders (e.g. CrMnFeCoNi [23–25], CrFeCoNi [26, 27] and AlCrFeNiCu [28]). Zhang *et al* [29] showed that a NbMoTaW RHEA could also be produced from a blend of elemental powders.

In contrast, LMD does not involve a powder bed; rather, the powder is introduced locally into the melt pool. This allows the composition of the powder blend to be changed during the process and material libraries, or material gradients, to be deposited for high-throughput compositional screening. Therefore, LMD can be used to explore the effects of compositional variations, characterize their properties for potential structural applications, and fabricate components with complex 3D geometries. So far, LMD has been used to produce HEAs starting with either a pre-alloyed powder or a blend of elemental powders. The following HEA systems were investigated: CrMnFeCoNi starting with a pre-alloyed powder [30–34]; and CrFeCoNiCu [35], AlSiTiVCr [36], $Al_2CrFeNiMo_x$ [37], $AlSiTiCrFe_6CoNi$ [38], $Al_xCrFeCoNiCu$ [39], $Al_xCrFeCoNi$ [40–42], AlCrFeCoNi/AlCrFeNiTa [43] and CrMnFeCoNi [44] starting with blends of elemental powders. However, compositional gradients (alloy libraries) have not been investigated in the literature, probably due to the challenge of precisely controlling alloy composition and processing HEAs using LMD.

LMD of RHEAs starting with blends of elemental powders is even more challenging due to their high melting points as well as the large differences between the melting temperatures of certain constituent elements. Its feasibility was first demonstrated by Dobbelstein *et al* [45] for MoNbTaW. Since then, LMD of RHEAs has attracted increasing interest (e.g. TiZrNbMoW [46], TiZrNbHfTa [47], TiZrNbTa [48], NbMoTaW [49–51]). In the remainder of this paper presents the potential and limitations of LMD for combinatorial materials research.

3. Experimental procedure

3.1. Experimental setup

All RHEAs were produced by LMD of elemental powder blends on a 3 mm-thick Ti substrate using a fiber laser with a spot diameter of ∼5 mm and a gaussian beam profile. The experimental setup is illustrated in figure 1. A process chamber was designed to perform LMD in an argon (Ar) atmosphere to minimize oxidation. The upper part of the setup is comprised of a laser processing head that includes a camera, focusing optics, and a powder nozzle, while the bottom part contains the sample fixed on a holder, figure 1. The two parts are connected by a sealed, flexible, and heat resistant silicone coated polyamide fabric to allow movement of the laser processing head relative to the specimen in 3D.

After positioning the sample and closing the chamber, the LMD system was purged with Ar for 2 min at a flow rate of 9 l min^{-1}. The same Ar flow rate was used to carry the powder blend into the melt pool. The Ar stream exits the chamber

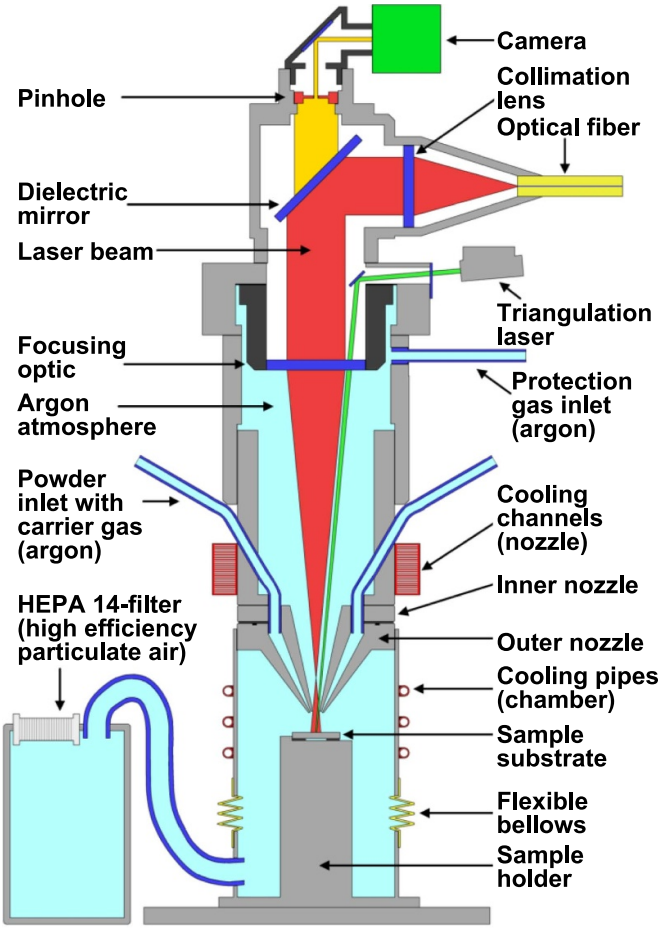

Figure 1. Experimental LMD setup.

through a silicon tube and a particle filter. Flowing water was used to dissipate heat and cool the nozzle and chamber. A green pilot laser was attached at a small angle to the optical beam path of the process laser and focused on the sample. In combination with the camera, a triangulation sensor monitored the height of the sample.

3.2. LMD geometry and procedure

Unlike most LMD geometries, which consist of horizontal weld seams, our samples were built vertically by stacking spot welds on top of each other. Columnar samples were produced by repeating the LMD steps illustrated in figure 2 and described next. (1.) (Deposition Phase): a local melt pool was created for 3 s with a laser power of 1200 W. This melt pool was initially located on the substrate, and moved to the top of each deposited layer as the sample was built. The powder stream was focused by a powder nozzle onto the melt pool where it melts. (2.) (Cooling Phase): the laser beam and powder stream were turned off for 1 s. (3.) (Remelting Phase): the laser beam (1200 W, 3 s) melted the top of the sample a second time without any powder flow. This step is necessary to fully melt and mix the high-melting elements Nb and Ta. Furthermore, during this third step, the underlying structure (below the melt pool) was annealed in the solid-state, which homogenized the dendritic microstructure of the deposited layers. (4.) (Cooling Phase): This step dissipated the heat that accumulated in the powder nozzle, sample holder, and the sample itself during the previous steps. Excessive overheating of the sample leads to heterogeneous 'melt-down' in which the melt pool diameter broadens, resulting in possible overflow down the sides of the columnar sample, like wax dripping down a lighted candle. Therefore a cooling period of 15 s was included. After this four-step sequence, the processing head was raised by ~300 μm, which corresponds to the thickness of each deposited layer, and the entire process was repeated. The thickness of each deposited layer depends slightly on the alloy composition; therefore, the height of the sample was monitored with the camera as well as the pilot laser, and the position of the processing head was manually adjusted.

3.3. Powder blend characteristics and preparation

The powder quality is of prime importance for additive manufacturing. The shape and size distribution of the particles strongly affect the flowability and focusability of the powder. Spherical particles with a size distribution of 20–150 μm are suitable for LMD [52] and this size distribution is mostly used. However, the availability of such refractory-element powders is limited and we used what we could find. Secondary electron (SE) micrographs of the powders used in the present work are shown in figure 3. Titanium (Ti) alloys are well established in the field of additive manufacturing; consequently, spherical elemental Ti powder were easily acquired (see figure 3). We were also able to purchase spherical, elemental zirconium (Zr) powder. In the case of Nb and Ta, two different types of powders were used to investigate the effect of particle morphologies on processability by LMD. The first set of Nb and Ta powders had irregular shapes (Nb^1 and Ta^1 in figure 3 and table 1). Such particles do not flow as smoothly as spherical particles, but they can still be used for LMD when mixed with spherical powders. Progress in plasma densification technologies recently resulted in the introduction of new spherical Nb and Ta powders (Nb^2 and Ta^2) that have the additional advantage of lower oxygen contents. The as-received Ta^2 powder with an initial particle size distribution of 10–63 μm was sieved to remove particles smaller than 25 μm to avoid demixing in the powder blend. The availability of hafnium (Hf) powder is extremely limited, mainly due to its high price, high melting point, high reactivity with oxygen, and the lack of applications. At the beginning of this study, an Hf^1 powder with irregular flake-shaped particles smaller than 15 μm was used. Due to its pyrophoric nature, this powder is shipped immersed in water. Upon receipt, it was removed from the water, dried at room temperature in air, and processed by LMD. This procedure, shown in a previous study [47], results in equiatomic $TiZrNb^1Hf^1Ta^1$ specimens with large pores near the substrate, presumably a result of degassing the remaining water, see figure 3 of [47]. To overcome this problem in the present study, the Hf^1 powder was dried in air on a heating plate at 80 °C for at least 24 h and then mixed with the other elemental powders. Finally, each powder

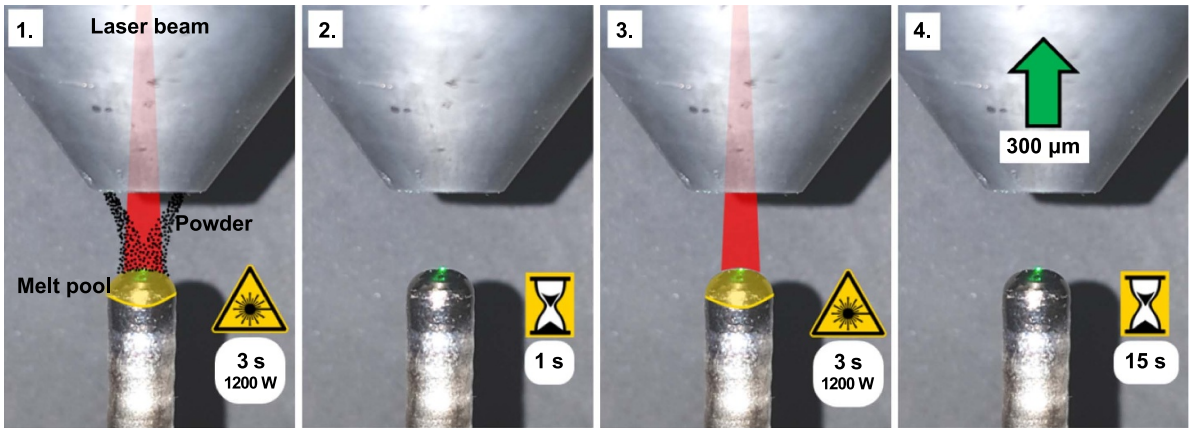

Figure 2. Illustration of the spot weld sequence for columnar build-up.

blend (∼7 g) was dried in air on a heating plate at 80 °C for at least 2 h before LMD. This procedure significantly reduces the porosity in TiZrNb^{1}Hf^{1}Ta^{1} specimens produced by LMD, as will be shown later. We were also able to purchase a small quantity (30 g) of a more suitable Hf^{2} powder for LMD—this powder was not immersed in water for shipping. The second Hf^{2} powder consists of broken particles with irregular shapes and sizes ranging from 44 μm to 250 μm, see figure 3 and table 1.

The oxygen (O) and nitrogen (N) contents of all powders, except the Hf^{2} powder, whose available quantity was too small, as well as those of some additively manufactured specimens were measured by the company *revierlabor GmbH* by carrier gas hot extraction. The oxygen contents of most of the powders are between 0.19 at.% and 0.73 at.%, and their nitrogen contents are between 0.01 at.% and 0.05 at.% (see table 1). In contrast, the oxygen (7.05 at.%) and nitrogen (3.06 at.%) levels in the Hf^{1} powder are significantly higher. Even though the interstitial concentrations of the Hf^{2} powder could not be directly measured, they were estimated based on their contents in two different alloys produced by LMD using this powder. The corresponding estimates are given in table 1. Compared to the first powder, the Hf^{2} powder has a reduced but still elevated oxygen concentration (5.30 at.%), while its nitrogen content (0.06 at.%) is significantly lower. Since the two Hf powders (Hf^{1} and Hf^{2}) exhibit different interstitial concentrations, this specificity was used in the present work to study their effects on processability by LMD, phase stability, and mechanical properties using two powder stocks: stock 1 (interstitial-rich: Ti, Zr, Nb^{1}, Hf^{1}, Ta^{1}) and stock 2 (interstitial-lean, Ti, Zr, Nb^{2}, Hf^{2}, Ta^{2}).

3.4. Effect of powder morphologies on processability

The powder blend from stock 1 is shown in the left image of figure 4, which is an energy-dispersive x-ray spectroscopy (EDX) elemental map superimposed on an SE micrograph. In our feeding system, the powder flows by gravity from a storage container into the groove of a rotating disc where it is transported by the Ar gas stream to the powder nozzle. However, the powder blend from stock 1 could not be fed in this manner because it did not flow easily. This occured because the small Hf^{1} particles stuck to the larger ones, filling the space between them. To feed the stock 1 powder blend, the powder feeder was modified by inserting a vibratory module between the storage container and the rotating disc. The vibratory module does not influence the powder feed rate, as the feed rate is defined by the groove size and the rotation speed of the disc. This construction allowed us to successfully produce specimens by LMD using the powder blend from stock 1.

The powder blend from stock 2 is shown in the right image of figure 4. Due to its more homogeneous particle size distribution, this blend had good flowability and could be fed into the powder nozzle without the vibratory module. When preparing the powder blends, each of the individual powder constituents and the final blend was weighed using a high-precision scale.

The nominal alloy composition differed from the actual composition of the deposited alloy for several reasons, for details see [48]. The compositions of the powder blends were iteratively modified following the procedure described in [47, 48]. For example, to obtain an equiatomic alloy, the blend composition used for stock 1 was $Ti_{16.7}Zr_{17.3}Nb_{19.9}Hf_{24.8}Ta_{21.3}$ while that for stock 2 was $Ti_{17.7}Zr_{18.4}Nb_{21.2}Hf_{20.1}Ta_{22.6}$. The end concentrations were also iteratively modified, and the intermediate alloy compositions were interpolated between these values to obtain concentration gradients, for more details see [48].

For an extensive analysis of *in-situ* alloying of refractory TiZrNbHfTa RHEAs produced by LMD, and the effects of various factors on processability, phase stability, microstructures and mechanical properties, the following compositions were considered. (a) To qualitatively assess the role of each element, five *compositionally graded* TiZrNbHfTa RHEAs were produced by changing the composition of one element from 15 to 40 at.% while maintaining the other elements at equimolar levels. For example, Ti-isopleth, $Ti_yZr_{25-y/4}Nb_{25-y/4}Hf_{25-y/4}Ta_{25-y/4}$, with a composition range of $15\% < y < 40\%$ was investigated. The compositionally graded Ti-isopleth specimen was fabricated by depositing five different powder blends, $Ti_{13.3}Zr_{21.7}Nb_{21.7}Hf_{21.7}Ta_{21.7}$ on the substrate followed by $Ti_{20}Zr_{20}Nb_{20}Hf_{20}Ta_{20}$, $Ti_{26.7}Zr_{18.3}Nb_{18.3}Hf_{18.3}Ta_{18.3}$, $Ti_{33.3}Zr_{16.7}Nb_{16.7}Hf_{16.7}Ta_{16.7}$,

Table 1. Physical properties of the used elements and powder characteristics.

Elements	Melting point[a] (°C)	Boiling point[a] (°C)	Crystal structure (RT)	Oxygen content[b] (at.%)	Nitrogen content[b] (at.%)	Particle size (μm)	Particle shape	Supplier
Ti	1668	3287	hcp	0.48	0.03	<106	spherical	Alfa Aesar
Zr	1855	4409	hcp	0.73	0.01	45–90	spherical	TLS Technik
Nb^1	2477	4744	bcc	0.42	0.01	45–75	irregular	TANIOBIS
Nb^2				0.19	0.05	63–105	spherical	TANIOBIS
Hf^1	2233	4603	hcp	7.05	3.06	<15	irregular	Nanoshel[c]
Hf^2				5.60[d]	0.01[d]	44–250	irregular	Alfa Aesar[d]
Ta^1	3017	5458	bcc	0.62	0.03	45–90	irregular	TANIOBIS
Ta^2				0.45	0.03	10–63	spherical	TANIOBIS

[a]Melting and boiling points from CRC Handbook of Chemistry and Physics, 90th edition, David R Lide
[b]Oxygen and nitrogen contents were measured by carrier gas hot extraction (CGHE) at *revierlabor GmbH*.
[c]Hf^1 powder was delivered under water due to its pyrophoric nature.
[d]Available amount of Hf^2 powder was only 30 g. Oxygen and nitrogen contents were not measured but indirectly estimated from the produced $TiZrNb^2Ta^2$ and $TiZrNb^2Hf^2Ta^2$ alloys (see table 2).

and $Ti_{40}Zr_{15}Nb_{15}Hf_{15}Ta_{15}$. All of the compositionally graded specimens were produced from the stock 1 powder blends because the quantity of powder stock 2 (especially Hf^2) was too limited. (b) To investigate the role of the interstitial elements oxygen (O) and nitrogen (N) on compression behavior, compression specimens were machined from *single-composition* samples of powder blends. To vary the O and N concentrations, powder blends from stock 1 (interstitial-rich) and stock 2 (interstitial-lean) were used to produce the equiatomic $Ti_{20}Zr_{20}Nb_{20}Hf_{20}Ta_{20}$ alloy. To further investigate the mechanical properties of compositions with low interstitial contents between 0.5 and 2 at.%, additional *single-composition* TiZrNbHfTa RHEAs were produced by LMD using the stock 2 powder. These alloys included: $Ti_{27}Zr_{27}Nb_{27}Hf_{9.5}Ta_{9.5}$, $Ti_{42}Zr_{22}Nb_{22}Hf_7Ta_7$, $Ti_{22}Zr_{42}Nb_{22}Hf_7Ta_7$, and $Ti_{22}Zr_{22}Nb_{42}Hf_7Ta_7$. (c) To study the effects of the liquidus temperature and the solidification range, the equiatomic refractory medium-entropy alloys (RMEAs) $Ti_{33.3}Zr_{33.3}Nb_{33.3}$, $Zr_{33.3}Nb_{33.3}Ta_{33.3}$, and $Ti_{25}Zr_{25}Nb_{25}Ta_{25}$ with low interstitial contents were prepared from the stock 2 powder.

3.5. Sample preparation and material characterization

The samples produced by LMD were cut longitudinally, embedded in epoxy, ground with silicon carbide (SiC) abrasive papers to a grit size of 8 μm, and polished for 1 h using a 1:1 vol.% suspension of 0.04 μm colloidal silica and hydrogen peroxide. Chemical compositions and microstructures were analyzed using these longitudinal sections at several locations along the growth direction. For more details about this procedure, refer to [47]. The chemical composition along the growth axis of the LMD samples was measured by EDX in a scanning electron microscope (SEM) of type Zeiss EVO MA 15 operated at an accelerating voltage of 20 kV. Phase and texture analyses were performed using large-area electron backscatter diffraction (EBSD) maps (consisting of ~100 individual EBSD maps) in an SEM of type Jeol JSM—7200F using an accelerating voltage of 30 kV, a probe current of 15 nA and a step size of 5 μm. The Vickers microhardness was measured along the full height of the samples with a hardness tester of type KB 30 and a load of 1 kgf. The hardness at a specific height along the growth direction was the average of three indents. From each single-composition specimen, two cylindrical compression samples (4 mm diameter × 7 mm height) with loading axes parallel to the growth direction were machined on a lathe. Compression tests were performed using a Zwick Roell XForce Z100 machine at room temperature using a nominal strain rate of 0.001 s^{-1}. To minimize friction during the compression tests, a molybdenum disulfide (MoS_2) grease was applied to the platens before deformation.

4. Results and discussion

Sections 4.1 and 4.2 describe the microstructures and properties of *single-composition* equiatomic samples after LMD. Section 4.3 discusses a few key factors affecting the processability of RHEAs and RMEAs by LMD. Section 4.4 presents the interstitial levels of the alloys. Section 4.5 builds on this knowledge by introducing the high-throughput synthesis of *compositionally graded specimens* and the screening of their microstructures and mechanical properties. Section 4.6 discusses the mechanical data obtained from the single-phase alloys to establish the effects of microstructure, chemistry, and interstitial-concentration, on strength. Our results are summarized in section 5, and the potentials and limitations of LMD to produce RHEAs are discussed in section 6.

4.1. Quinary TiZrNbHfTa RHEA

The quinary equiatomic $TiZrNb^2Hf^2Ta^2$ RHEA was deposited from the interstitial-lean stock 2 powder on a Ti substrate. An inverted optical image of its longitudinal section is shown in figure 5(a) where three different types of structural defects can be observed. (a) At the bottom of the sample, Nb- and Ta-particles can be found in the mixing zone between the alloy and the substrate and at the edges of the first deposited layers,

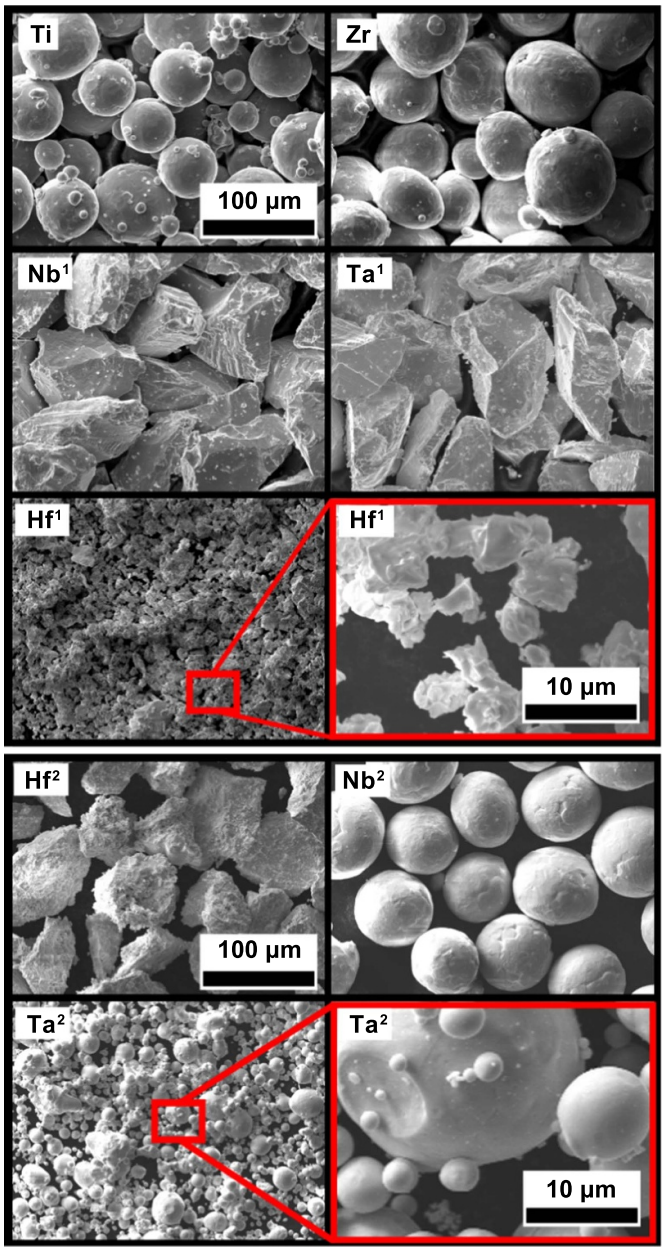

Figure 3. Representative SE images of the powders used in the present work. Powder blends were prepared from two types of powders to control the oxygen and nitrogen contents in the specimens produced by LMD and investigate the effect of powder morphologies on processability, phase stability, and mechanical properties. All images except the ones framed in red were recorded with the same magnification. This means that the scale bar stating 100 μm belongs to all non-highlighted images. For more details see the text.

see the EDX maps in figure 5(g). At the beginning of LMD, the melt pool temperature is relatively low and its lifetime is short due to its proximity to the substrate, which acts as a heat sink. As a result, mixing elemental powder particles, especially those with the highest melting points, is not perfect; and un-melted particles remain close to the substrate. The elemental powder particles tend to mix better at greater specimen heights. The temperature, lifetime, and size of the melt pool increase as the specimen height increases, which means that the deposited alloy has a lower heat flow than the substrate. (b) Interdendritic shrinkage porosity develops at the top of the sample, in the upper part of the melt pool that solidifies last (a higher magnification image can be found in figure 5(c)). (c) A few small pores are visible in the middle of the sample.

To investigate the homogeneity of the specimen at the millimeter-scale, EDX measurements were taken at various locations spaced 150 μm apart along the growth axis of the LMD-specimen. Each measurement was averaged over an area that was 2000 μm broad and 150 μm wide along the axis of the cylindrical specimen. The corresponding concentration profile is shown in figure 5(b) where the concentrations of the different alloying elements are plotted as a function of the distance from the top of the sample ($x = 0$). The upper part of the specimen ($0 < x < 7.5$ mm) shows a homogeneous, nearly equiatomic composition. In the lower part, some deviations of ± 4 at.% are apparent along with intermixing of the Ti substrate and the alloy at $14 < x < 17.5$ mm. Figure 5(b) also shows the hardness profile as black data points (right y-axis). The hardness is relatively homogeneous and has an average value of $\sim$350 HV1 for the region located between 0 mm and 15 mm, indicating that the deviation from equiatomic composition does not have a significant effect on strength. The hardness decreases with increasing Ti concentration with a minimum value of $\sim$150 HV1 in the substrate at $x = 18$ mm.

The green frames labeled *c* through *g* in figure 5(a) mark the regions of interest where backscatter electron (BSE) micrographs were recorded (figures 5(c))–(g)) and EDX analyses (figures 5(d-EDX), (f-EDX) and (g-EDX) maps) were performed. Figure 5(c) was taken at the top of the sample where the last melt pool solidified. This region shows a coarse dendritic microstructure with shrinkage porosity (see the black areas in figure 5(c)). Figure 5(d) shows a clearer image of the dendritic microstructure taken 2.5 mm away from the top of the specimen. EDX elemental maps are displayed in figure 5(d-EDX) maps. The dendrites are enriched in Ta (the element with the highest melting point), while the interdendritic regions are correspondingly enriched in Ti, Zr, and Hf. A dendritic microstructure can also be observed in figure 5(e) but its contrast is less pronounced than in figure 5(d). As one moves closer towards the substrate, the dendritic microstructure vanishes at distances $x > 4$ mm (figure 5(f), BSE micrograph and EDX maps). The bright areas within the darker matrix in figure 5(f) probably originated from surface deformation during sample preparation since the corresponding EDX elemental maps in figure 5(f) show a homogeneous chemical composition. The microstructural evolution from locations *c* to *f* shows that the dendritic microstructures were homogenized by solid-state interdiffusion during the deposition of successive layers (see section 4.5). In other words, as upper layers are deposited and remelted, the underlying solid layers with an initially dendric structure are annealed and homogenized as heat from the melt pool flows towards the substrate. Close to the Ti substrate at $14 < x < 17$ mm, an intermixing region where Nb and Ta particles were not fully melted during the LMD process can be seen in the BSE and EDX maps, shown in figure 5(g).

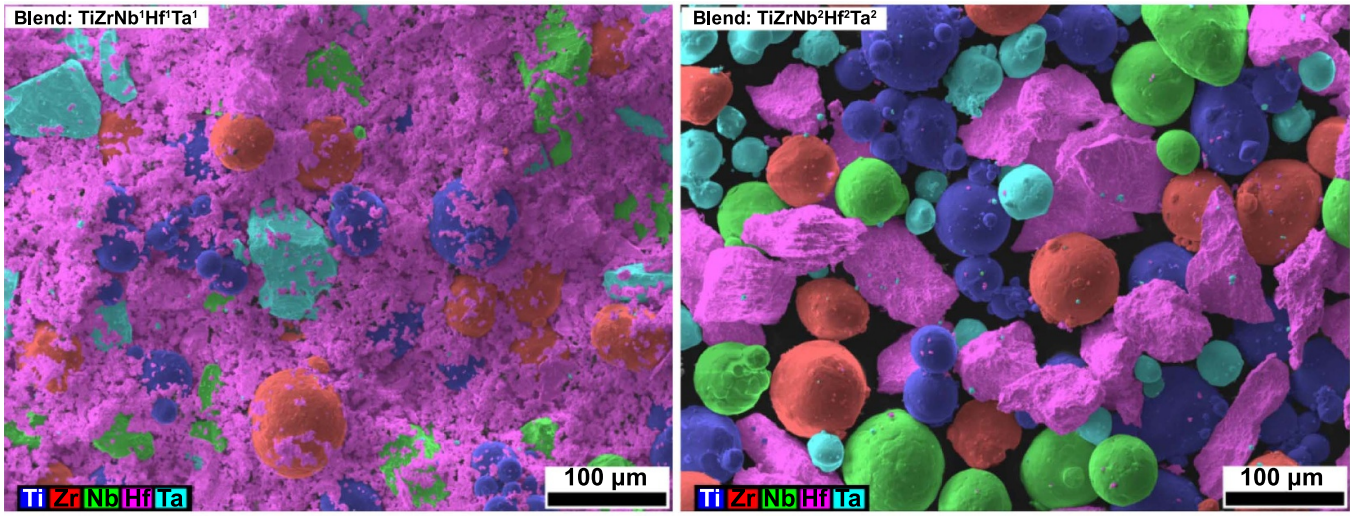

Figure 4. Powder blends from stock 1 (left) and stock 2 (right) with poor and good flowability, respectively.

Similar analyses were also performed for an equiatomic $TiZrNb^1Hf^1Ta^1$ RHEA that was prepared from the interstitial-rich stock 1 powder. The specimen was found to have a microstructure similar to that of the interstitial-lean $TiZrNb^2Hf^2Ta^2$ RHEA, except for the presence of a low volume fraction of small precipitates along the grain boundaries. Additional information regarding such precipitates as well as the parameters promoting their formation, will be presented in section 4.5. The $TiZrNb^1Hf^1Ta^1$ alloy was found to be much harder than the $TiZrNb^2Hf^2Ta^2$ RHEA indicating that O and N contents significantly affect the strength of the quinary equiatomic alloys. These aspects will be discussed in more detail in section 4.6.

4.2. Microstructure of the TiZrNbTa RMEA

Analyses similar to those mentioned above were performed on the quaternary TiZrNbTa RMEA produced from the stock 2 powder, using the same LMD parameters as those used to produce the quinary $TiZrNb^2Hf^2Ta^2$ RHEA. The results are presented in figure 6, using the same layout as figure 5 for ease of comparison of the macro-/micro-structures. Similar defects are observed in the quaternary and quinary alloys, but the TiZrNbTa sample contains large pores (∼1 mm diameter) that coalesced to form large cavities. Most of these cavities are located along the central axis of the specimen and heterogeneously distributed along its height. At this stage, it is worth mentioning that the LMD process had to be interrupted after half of the specimen was grown (at $x \approx 9$ μm) due to the limited size of our powder container. After a refill, during which the specimen cooled for ∼3 min, the process was resumed and the second half of the specimen was built. While this interruption and cooling did not affect the porosity of the quinary TiZrNbHfTa alloy (figure 5(a)), it induced the formation of elongated pores along the transverse direction in the quaternary TiZrNbTa alloy at $x = 9$ mm. These pores probably resulted from the rapid heat dissipation that took place during the short interruption. Large cavities formed at $6 < x < 9$ mm but were absent at the top of the TiZrNbTa specimen. The reasons for the non-uniform distribution of pores along the height of the TiZrNbTa specimen will be discussed at the end of this section. While the overall composition of the specimen is roughly equiatomic, the large pores and cavities affected the local chemical composition, which is enriched in Ti and Zr and correspondingly depleted in Ta and Nb, see figure 6(b). A more detailed EDX analysis was carried out near the largest pore, and the corresponding elemental maps are displayed in figure 6(f). Here, the ∼100 μm thick matrix shell surrounding the pore is Ti- and Zr-rich and Nb- and Ta-poor.

Similar to what was observed in figure 5(c), interdendritic shrinkage porosity occured on the top of the TiZr-NbTa sample within the last solidified melt pool (see the black areas in figure 6(c)). However, the dendritic microstructure at the top of the TiZrNbTa sample shows a stronger contrast than that found in the quinary TiZrNbHfTa RHEA (compare figures 5(d) and 6(d)). The dendritic cores are enriched in the elements Nb and Ta with high melting points and have a composition of $Ti_{21}Zr_{15}Nb_{29}Ta_{35,}$ while the interdendritic regions are enriched in Ti and Zr ($Ti_{29}Zr_{35}Nb_{21}Ta_{15}$), similar to the composition found close to the largest cavities (at $6 < x < 7$ mm in figure 6(b)). Interestingly, while Nb was evenly distributed within the dendritic microstructure of the quinary RHEA (figure 5(d-EDX) maps), Nb concentrated at the dendritic cores in the quaternary TiZrNbTa alloy. Close to the substrate, high magnification images (not shown here) also showed the presence of partially homogenized dendritic microstructures. This is in contrast to the TiZrNbHfTa sample, in which the dendritic microstructures were fully homogenized along most of the specimen height, $4 < x < 17$ mm, indicateing that full in-process homogenization during LMD was not possible for the TiZrNbTa alloy.

To better understand the factors contributing to the macro- and micro-structural differences between the quaternary and quinary alloys, thermodynamic calculations were performed by Dr. J-P Couzinié from the 'Institut

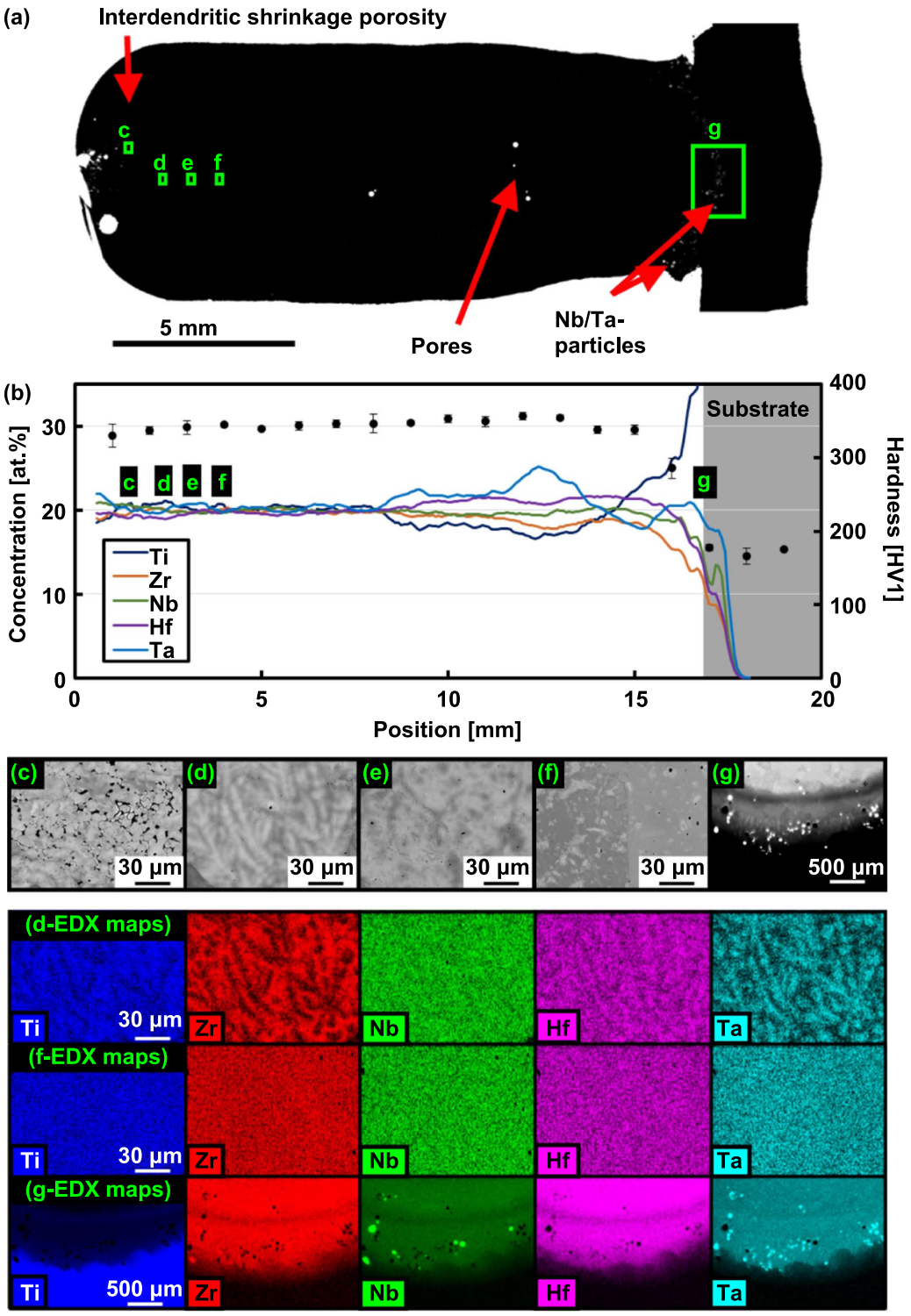

Figure 5. (a) Inverted optical image of the equiatomic **TiZrNbHfTa** RHEA produced with the interstitial-lean stock 2 powder. The green rectangles *c* through *g* highlight the regions of interest. (b) EDX concentration profiles (lines) of the constituent elements along the cylindrical axis of the specimen. Also shown in (b) is the hardness profile (right *y*-axis) represented by black dots with error bars. The position $x = 0$ indicates the top of the columnar specimen, and positions above ∼16 mm are located within the Ti substrate. (c–g) BSE micrographs showing the microstructural evolution along the growth axis of the specimen and corresponding EDX elemental maps. For more details refer to the text.

de chimie et des matériaux Paris-est, Thiais, France' (see the acknowledgments section) using CALPHAD software and the TCHEA4 database to compute the solidus and liquidus temperatures of these alloys. All liquidus temperatures and solidification ranges presented in the remainder of the paper for other alloys were obtained using the

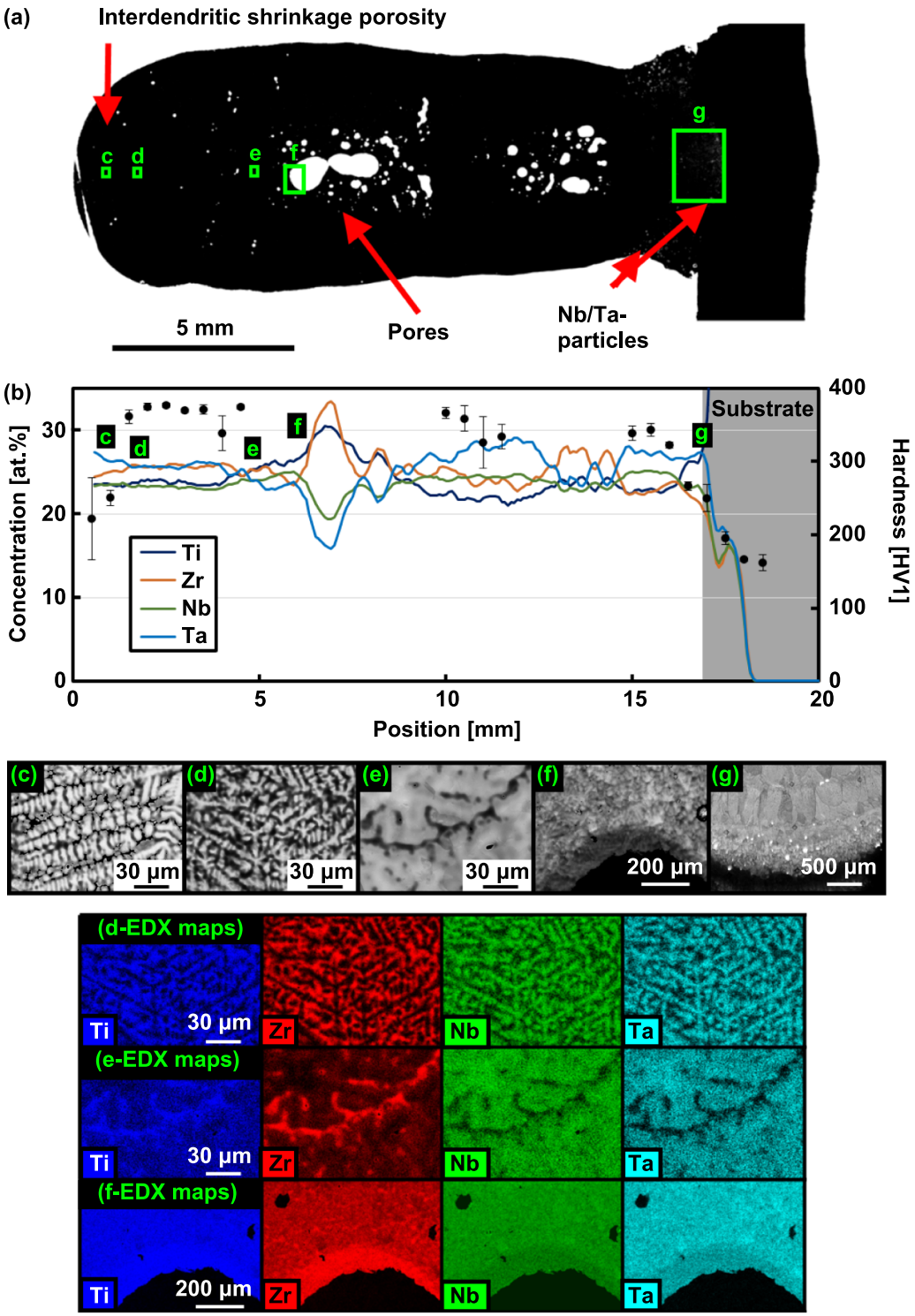

Figure 6. (a) Inverted optical image of the equiatomic **TiZrNbTa** RMEA produced with stock 2 powder, showing the presence of large pores. The green frames *c* through *g* show locations where detailed microstructural and chemical characterizations were performed. (b) The EDX concentration profiles of the constituent elements along the growth axis are shown as lines, and the hardness profile (right *y*-axis) is represented by black dots with error bars. The position $x = 0$ indicates the top of the specimen, and positions above ∼16 mm are located within the Ti substrate. (c–g) BSE micrographs and corresponding EDX elemental maps showing the microstructural evolution along the growth axis of the specimen. For more details see the text.

same procedure, and the data are provided in tables A1–A6 of the supplementary material (available online at https://stacks.iop.org/IJEM/3/015201/mmedia). Even though interstitials may affect solidus and liquidus temperatures, O and N are not included in the TCHEA4 database, so their contributions were neglected. The quinary TiZrNbHfTa and quaternary TiZrNbTa alloys solidify in temperature ranges of ∼1850 °C–2030 °C and ∼1790 °C–2090 °C, respectively.

Since the quaternary alloy has a wider solidification range (∼300 °C) than the quinary alloy (∼180 °C), the chemical partitioning during dendritic solidification is expected to be stronger in TiZrNbTa than TiZrNbHfTa. This expectation agrees with the experimental results, compare figures 5(d) and 6(d). Moreover, additional EDX line scans (not shown here) revealed that the concentration fluctuations within the dendritic microstructures for Ta are ±10 at.% in TiZrNbTa and ±4 at.% in TiZrNbHfTa. As the chemical partitioning during solidification is much stronger in the quaternary TiZrNbTa MEA, the cyclic heat treatments resulting from the LMD process are not sufficient enough to homogenize the dendritic microstructure.

Regarding the formation of porosity, as TiZrNbTa has a larger solidification range and a higher liquidus temperature than the quinary alloy, the former is expected to exhibit more porosity from dendritic shrinkage. A possible mechanism through which shrinkage porosity transforms into rounded pores will be treated in the next section. We now discuss possible reasons for the non-uniform distribution of pores and cavities in the quaternary TiZrNbTa alloy (figure 6(a)). At the beginning of the LMD process, the cooling rates are high and the melt pool has a relatively low temperature and short lifetime. Under these conditions, only the elements with the lowest melting temperatures are dissolved (e.g. Ti and Zr). The melt has a low liquidus temperature and a narrow solidification range, while the powder particles with high melting points (Ta and Nb) remain 'as is' (unmelted) in the structure. As the specimen grows, the distance between the melt pool and the substrate increases, heat accumulates in the specimen, and the melt pool temperature rises. When the melting temperature of Nb and Ta is reached (∼2 mm away from the substrate), these particles are dissolved in the melt pool. As a result, the liquidus temperature and solidification range drastically increase. Consequently, dendritic solidification becomes more severe and the viscosity of the melt pool increases, which together presumably promote the formation of pores due to one or more of the following mechanisms: (a) The temperature at the center of the melt pool is higher than at its periphery, which leads to inward solidification and may result in the formation of shrinkage porosity along the central axis of the specimen (where the last liquid solidifies). (b) Since the boiling temperature of Ti is only 270 °C above the melting temperature of Ta (table 1), we cannot exclude the possibility that some pores observed in TiZrNbTa (figure 6(a)) may be related to the evaporation of Ti, which may be trapped in the middle of the specimen due to the high viscosity of the melt pool. (c) A significant amount of dendritic shrinkage porosity was observed at the top of the specimen (figure 6(c)), and subsequent cyclic anneals during LMD may transform it into rounded pores (see next section). These mechanisms may result in the formation of pores in the region $11 < x < 15$ mm, see figure 6(a). The pores hinder heat flow in the specimen, and heat accumulates faster in the LMD specimen during its growth. As a result, the temperature and lifetime of the melt pool increase while the temperature gradient and cooling rate decrease. These conditions may suppress the formation of pores and large cavities at $9 < x < 11$ mm. As mentioned previously, heat dissipated when the LMD process was interrupted at $x = 9$ mm for 3 min. When the LMD process was resumed, the temperature gradient and cooling rate suddenly increased, which promoted the formation of porosity at $6 < x < 9$ mm. Finally, heat accumulated again as the specimen grew in height and large cavities disappeared at $x < 6$ mm. Together, these results suggest that heat accumulation plays a key role in the suppression of porosity and the homogenization of dendrites. Therefore, pre-heating the Ti substrate may be beneficial for processing refractory alloys with high liquidus temperatures and broad solidification ranges. Further work is needed to investigate this.

4.3. Effect of liquidus temperature and solidification range on processability and microstructures

The previous section showed that both the liquidus temperature and the solidification range play major roles in the processability of refractory alloys by LMD. To further study the effects of these parameters on sample size/shape, microstructure, and how porosity forms during LMD, two additional ternary equiatomic alloys with low (TiZrNb, $T_{liq} = 1827$ °C) and high (ZrNbTa, $T_{liq} = 2272$ °C) liquidus temperatures and narrow and broad solidification intervals (138 °C for TiZrNb and 365 °C for ZrNbTa) were investigated using the same set of processing parameters. The dimensions of the TiZrNb and ZrNbTa specimens produced by LMD from the stock 2 powder are strongly affected by their respective liquidus temperatures and solidification ranges. The TiZrNb specimen has a short height of ∼9 mm and a diameter of ∼7.5 mm, which exceeds the laser spot size, see figure 7(a). In contrast, the ZrNbTa sample has a greater height of ∼14 mm and a smaller diameter of ∼5 mm, the latter is comparable to the laser spot size, see figure 7(A). These results can be rationalized as follows: for constant processing parameters, an alloy with a low liquidus temperature has a low melt pool viscosity [53, 54]. As a result, the melt pool of the TiZrNb specimen spreads in the plane perpendicular to the growth direction. This behavior affects the final dimensions of the specimen, resulting in a large diameter and a short height. In contrast, the higher viscosity of ZrNbTa, due to its higher liquidus temperature, does not produce significant lateral spread of its melt pool. As a result, each deposited layer is thicker and the column diameter keeps roughly the same size as the laser spot.

The differences in liquidus temperatures and solidification ranges of the two alloys have a strong effect on porosity. While ZrNbTa with a high T_{liq} and a broad solidification interval presents a large number of pores, TiZrNb is almost devoid of pores. If we compare the structures of TiZrNbTa ($T_{liq} = 2088$ °C) and ZrNbTa ($T_{liq} = 2272$ °C) shown in figures 6(a) and 7(A), respectively, the pores in the quaternary alloy are much larger than those in the ternary alloy for a comparable solidification range (299 °C for TiZrNbTa compared to 365 °C for ZrNbTa). However, as mentioned previously since the boiling temperature of Ti is close to the melting point of Ta, the largest pores observed in TiZrNbTa (figure 6(a)) may be related to the evaporation of Ti. The evaporation of Ti in combination with the melt pool viscosity may also affect porosity. In other words, Ti may evaporate during LMD of the TiZrNb

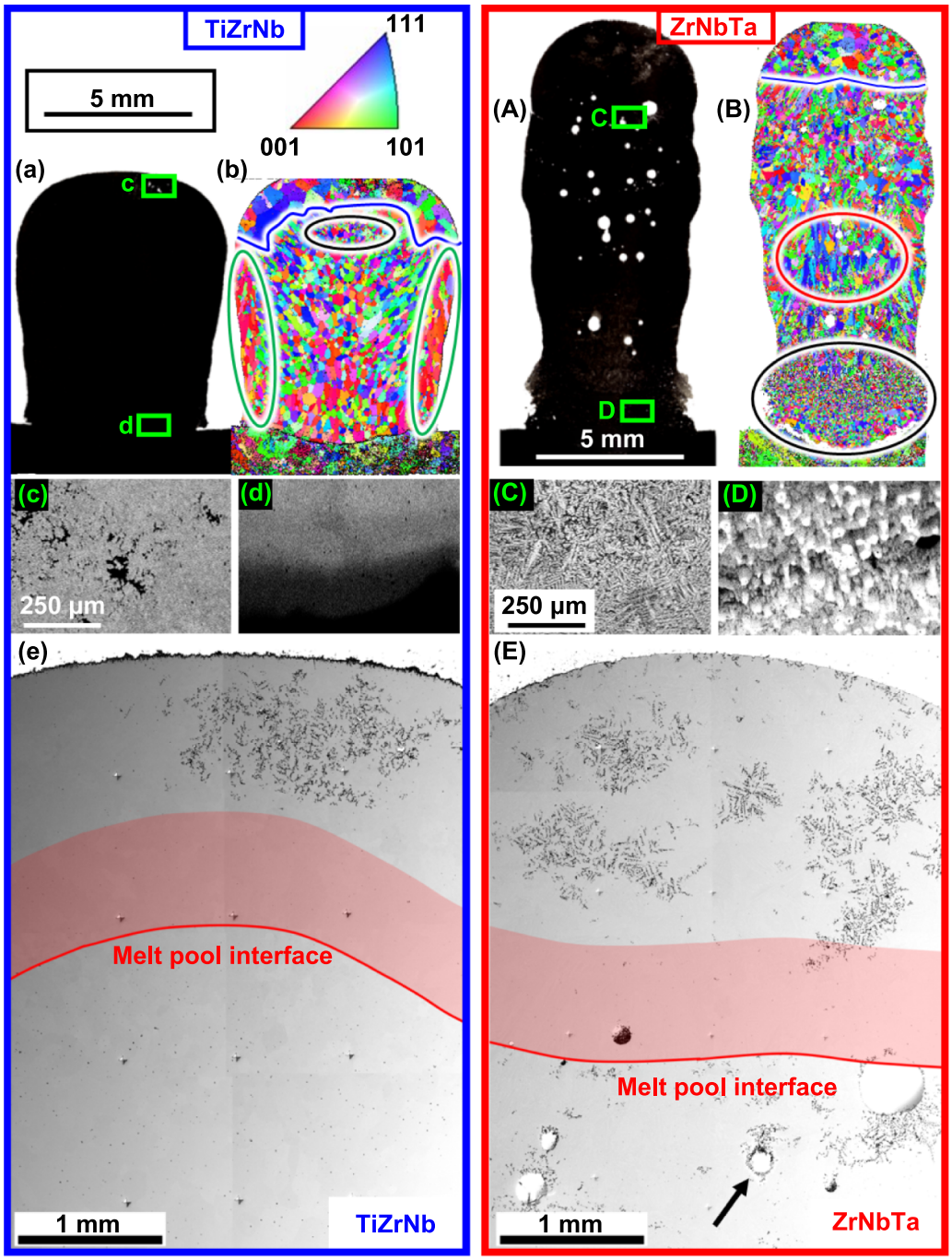

Figure 7. Comparison of the (micro/macro)-structures of two alloys with low (**TiZrNb**, left column) and high (**ZrNbTa**, right) liquidus temperatures and narrow (**TiZrNb**) and broad solidification intervals (**ZrNbTa**) produced by LMD with the stock 2 powder. (a) and (A) Inverted optical images of equiatomic TiZrNb and ZrNbTa samples, respectively, showing the effect of liquidus temperature and solidification range on sample geometry and structural defects. (b) and (B) Grain orientation maps where the colors indicate crystallographic orientations parallel to the growth direction displayed in the stereographic triangle in (b). (c)–(d) and (C)–(D) BSE micrographs recorded at the locations highlighted in (a) and (A), respectively. (e) and (E) Optical micrographs of the upper parts of the TiZrNb and ZrNbTa samples showing clusters of interdendritic shrinkage porosity and eventually pores. The red lines indicate the initial solid/liquid interfaces during the phase 1 deposition while the red areas show the regions that were not remelted during phase 3 (see LMD sequence in figure 2). If shrinkage porosity is present in a red area (e.g. (E) for ZrNbTa), it transforms into large pores during the successive deposition of layers by LMD.

alloy and could easily escape from the specimen since the Ti gas migrates through a melt pool with a low viscosity. In contrast, the denser melt pool of the TiZrNbTa specimen may trap the Ti gas during its rapid solidification.

Phase analysis was performed using EBSD over the complete surface area of the longitudinal sections. The corresponding phase maps (not shown here) revealed that the LMD specimens (TiZrNb, ZrNbTa as well as TiZrNbTa and TiZrNbHfTa)

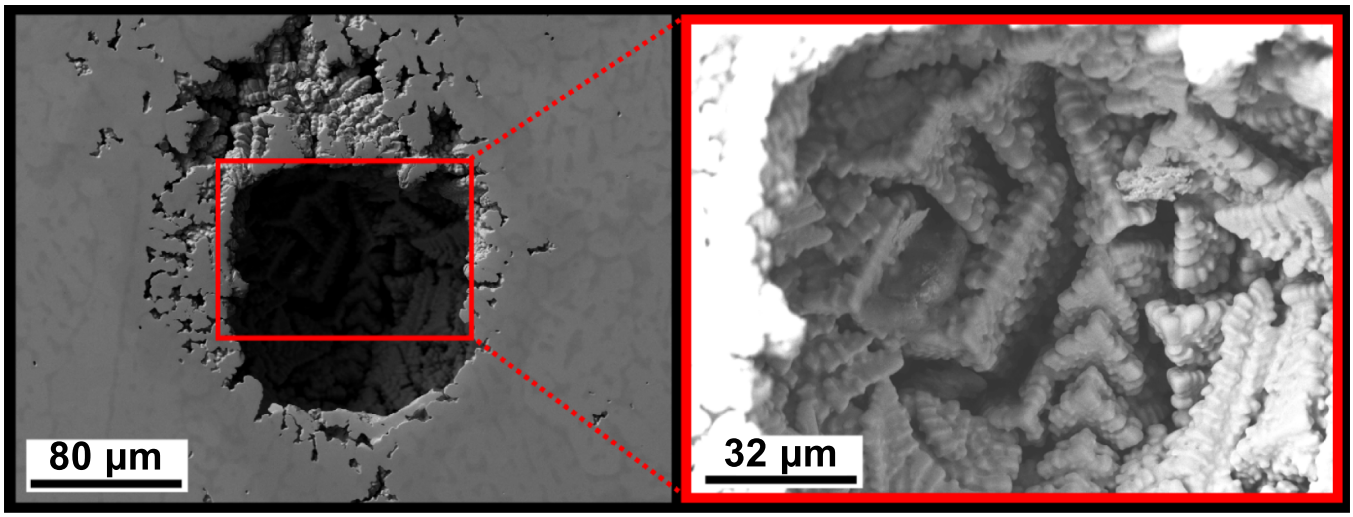

Figure 8. Microstructure of a spherical pore in the **ZrNbTa** specimen with a high liquidus temperature and a broad solidification range (This pore is indicated by a black arrow in figure 7(E)). Here dendrites are clearly visible at the surface of the pore.

were single-phase bcc while the Ti substrates were hexagonal close-packed (hcp). Large color-coded grain orientation maps of the samples are provided in figure 7(b, B) where individual crystallites are colored according to their crystallographic orientation relative to the growth (here vertical) axis. The upper part of the TiZrNb specimen in figure 7(b) presents two distinct microstructural features: Large equiaxed grains are visible at the top of the specimen above the blue line. In contrast, much smaller grains are visible within the black ellipse. These microstructures formed during the solidification of the last melt pool with the lower (black ellipse) and upper parts (above the blue line) exhibiting fine and coarse grain microstructures, respectively. In the lower parts of the TiZrNb specimen (figure 7(b)), the grains are smaller and equiaxed in the middle of the cylindrical specimen and become slightly elongated and larger as one moves from the center of the specimen towards its lateral surfaces. This is reminiscent of the grain structure in castings and welded metals where the grains near the edges, or the liquid-solid interface, are larger and elongated along the heat flow direction and smaller and equiaxed near the center. The TiZrNb alloy is not strongly textured except for the outer grains inside the green ellipses in figure 7(b), where the red color indicates that the <100> crystallographic directions of these grains are preferentially oriented along the growth direction. However, since microhardness testing was performed in the middle of the specimens and the narrow textured regions were removed during machining of the compression specimens, the mechanical data reported in section 4.6 are representative of polycrystals with near-random grain orientations. The grains of the ZrNbTa sample are generally smaller and have more irregular morphologies than those of TiZrNb. This is probably related to the fact that the solidification rates are higher in ZrNbTa than in TiZrNb since the former has a higher liquidus temperature than the latter. As in the TiZrNb alloy, ZrNbTa does not show a strong texture except for the area marked with a red ellipse in figure 7(B) where grains elongated along the growth direction exhibit a blue color indicating a slight <111> fiber texture. At the bottom of the sample, the ZrNbTa alloy shows very small grains in the region where Nb and Ta particles were not melted, see black ellipse in figure 7(C) and bright particles in figure 7(D). No compression specimens were produced from ZrNbTa because of its significant porosity.

We now compare the microstructures of the two alloys near the top and the bottom of the specimens, see locations c-d and C-D in the BSE micrographs in figure 7(a, A), respectively. While no obvious micro-segregation could be detected in the TiZrNb alloy (figure 7(c), (d)), clear dendritic microstructures were observed throughout the ZrNbTa alloy (figure 7(C), (D)). This difference is probably related to the higher liquidus temperature and solidification range of the latter alloy, which induces a higher solidification rate and a more pronounced dendritic microstructure. The different liquidus temperatures are also consistent with the microstructures observed at the bottom of the specimens. While the elemental powders were fully mixed in the TiZrNb specimen with a low T_{liq}, the temperature of the first melt pools was not high enough to dissolve the Nb and Ta particles in the ZrNbTa specimen, figure 7(D). The EDX concentration and hardness profiles along the built-up direction of the TiZrNb and ZrNbTa RMEAs can be found in figure A1 (supplementary material).

We have seen that pores are more likely to appear when the alloy has a high liquidus temperature and a broad solidification range. This observation indirectly shows that interdendritic shrinkage porosity may play a role in the formation of pores. For this reason, interdendritic shrinkage porosity was examined more closely. In all of the alloys investigated here, the microstructures of the last solidified melt pools were found to be dendritic. Moreover, non-uniformly distributed clusters of interdendritic shrinkage porosity were observed in all of them (e.g. figure 7(e, E)) for TiZrNb and ZrNbTa, respectively). Most of these clusters appear in the upper part of the melt pool, which solidifies with an equiaxed dendritic microstructure. While the clusters are located close to the

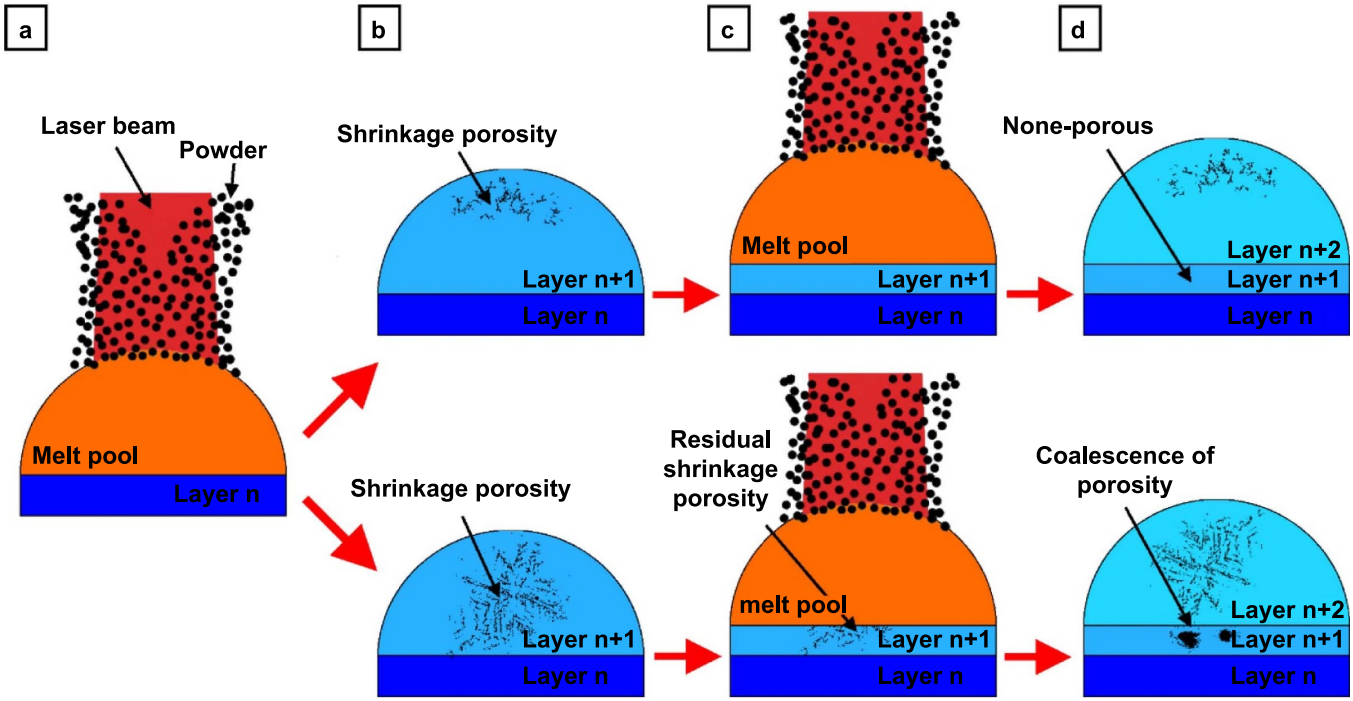

Figure 9. One of the mechanisms leading to the formation of spherical pores in specimens with high liquidus temperatures and broad solidification ranges (lower row) while samples with low liquidus temperatures and narrow solidification ranges remain pore free (upper row). (a) Deposition of the $n + 1$ layer. (b) After solidification of this layer, clusters of interdendritic shrinkage porosity form within the last solidified melt pool and their distribution depends on the liquidus temperature and solidification interval. The clusters are located at the top of the last solidified melt pool in alloys with low liquidus temperatures and narrow solidification ranges (upper row) while they are present further away from the top in alloys with high liquidus temperatures and broad solidification intervals (lower row). (c) During the deposition of the $n + 2$ layer, the clusters of shrinkage porosity are either completely remelted and eliminated (upper row) or trapped in the solidified microstructure (lower row). (d) As a result of the heat flowing from the melt pool towards the substrate, the clusters coalesce into larger spherical pores, minimizing the interfacial energy.

liquid/gas interface in TiZrNb (∼1 mm away for the top of the LMD specimen, figure 7(e)), they are present further away (∼2.5 mm) in ZrNbTa, see figure 7(E). While spherical pores are nearly absent in TiZrNb, some pores formed in the vicinity of the clusters present in ZrNbTa. One of these pores is marked with a black arrow at the bottom of figure 7(E), and its microstructure is magnified in figure 8 where dendrites are clearly visible at the surface of the pore.

Figure 9 schematically illustrates the effect of heterogeneous spreading of the melt pools on the transformation of interdendritic shrinkage porosity into spherical pores in the final LMD structure. The TiZrNb alloy has a low liquidus temperature, and the melt pool has a low viscosity and spreads laterally, resulting in thin deposited layers. The clusters of interdendritic shrinkage porosity are located in a narrow region close to the top of each deposited layer (see the upper row of figure 9(b)). This region is remelted during the deposition of the next layer, which eliminates the clusters (figure 9(c)). As a result, both layers n and $n + 1$ (figure 9(d)) are devoid of spherical pores. In contrast, the higher liquidus temperature, melt pool viscosity, and solidification interval combined with the faster solidification rate of the ZrNbTa alloy produce a higher number of clusters of interdendritic shrinkage pores (figure 9(b), lower row). If some of these clusters are located outside the melt pool of the next deposited layer, porosity is trapped in the solidified structure (figure 9(c), lower row). As heat accumulates during the successive deposition of additional layers, the clusters of interdendritic porosity coalesce into large spherical pores, decreasing the interfacial energy (figure 9(d), lower row).

4.4. Oxygen and nitrogen contents in RHEAs and RMEAs after LMD

The O and N concentrations in the equiatomic $TiZrNb^1Hf^1Ta^1$ alloy produced from the stock 1 powder were determined by a commercial analysis laboratory to be 1.89 at.% and 0.76 at.%, respectively (see table 2). Assuming that the interstitial impurities in the starting elemental powders (table 1) ended up entirely in the LMD structures, we can compute the O and N contents in the equiatomic alloy as 1.85 at.% and 0.63 at.%, respectively (table 2). These calculated values are comparable to the measured values, indicating that the interstitials are introduced into the alloy primarily from the elemental powders. The quaternary equiatomic $TiZrNb^2Ta^2$ RHEA is found to contain much lower quantities of O and N (0.66 and 0.09 at.%, respectively), which may be compared to the expected values (0.46 at.% for O and 0.03 at.% for N). These two results indicate that relatively low concentrations of O (0.04–0.2 at.%) and N (0.06–0.13 at.%) are introduced during LMD. Most of the O and N in the specimen originated from the elemental powders. As mentioned previously, the

Table 2. Interstitials concentration in deposited equiatomic alloys determined experimentally by carrier gas hot extraction (*revierlabor GmbH, Essen, Germany*). Calculated (mean value) concentrations assume that the interstitials originate from the elemental powders.

Alloy	S (at.%)	H (at.%)	O (at.%)	N (at.%)	C (at.%)
$TiZrNb^1Hf^1Ta^1$—exp	0.01	0.07	1.89	0.76	0.05
$TiZrNb^1Hf^1Ta^1$—calc.	—	—	1.85	0.63	—
$TiZrNb^2Hf^2Ta^2$—exp	—	—	1.59	0.08	—
$TiZrNb^2Ta^2$—exp	—	—	0.66	0.09	—
$TiZrNb^2Ta^2$—calc.	—	—	0.46	0.03	—

interstitial contents of the Hf^2 powder could not be determined due to the small quantity of available powder. However, an equiatomic $TiZrNb^2Hf^2Ta^2$ was produced by LMD using the stock 2 powder, and its O and N contents were found to be 1.59 at.% and 0.08 at.%, respectively. Assuming that LMD introduces ∼0.1 at.% of O and N and that their concentrations in the elemental powders remain in the specimen after LMD, the interstitial contents of the Hf^2 powder were estimated to be 5.6 at.% O and 0.01 at.% N, see table 1. In the remainder of the present study, the interstitial concentrations of all RHEAs were estimated using the above assumptions with the interstitial contents listed in table 1.

4.5. High-throughput synthesis and screening of compositionally graded structures

Based on the knowledge gained from sections 4.1–4.4, we now investigate compositionally graded specimens for high-throughput screening of their microstructures and hardnesses. These specimens were produced from the stock 1 powder using the same set of parameters that were used for the equiatomic TiZrNbHfTa RHEA. The compositionally graded structures and the equiatomic TiZrNbHfTa specimens have different heights, ∼40 mm and ∼17 mm, respectively. A concentration profile along the growth direction of a compositionally graded columnar sample is presented in figure 10(a). The Ti concentration decreases from ∼40 at.% at the top of the columnar sample ($x = 0$ mm) to ∼13.3 at.% at the sample/substrate interface ($x = 37$ mm). The other elements remain in roughly equiatomic proportions and each of their concentrations increase from ∼15 at.% to ∼21.7 at.%. The O and N concentrations within the specimen were estimated to increase linearly from 1.6 at.% to 2.1 at.% and 0.6 at.% to 0.8 at.%, respectively, between the $Ti_{40}Zr_{15}Nb_{15}Hf_{15}Ta_{15}$ and $Ti_{13.3}Zr_{21.7}Nb_{21.7}Hf_{21.7}Ta_{21.7}$ alloys, assuming that the interstitials present in the elemental powders (see table 1) remain after processing, and that LMD introduces 0.1 at.% O and 0.1 at.% N. Distinct segments are visible in figure 10(a) corresponding to the five different powder blends (e.g. the Ti-concentration profile has a five-step staircase shape). The slight slope at the edge of each step indicates that intermixing took place between the layers, which is typical for successively laser-welded samples with dissimilar compositions. The hardness profile (right y-axis, black data points in figure 10(a)) shows the same segmentation as the concentration profile. Average hardness within individual segments are 450 HV1 (13.3 at.% Ti), 466 HV1 (20 at.% Ti), 441 HV1 (26.7 at.% Ti), 417 HV1 (33.3 at.% Ti), and 392 HV1 (40 at.% Ti), with a low scatter of ∼5 HV1 within each. The highest hardness is found for the equiatomic composition and the lowest hardness for the Ti-rich composition. The unalloyed Ti substrate, $x > 37$ mm, has the lowest hardness of all (150 HV1). At the top of the sample ($x < 1$ mm), the local hardness is much lower with large scatter due to the presence of interdendritic shrinkage porosity, typical of all of the specimens investigated in the present work (e.g. figure 7(e)). Note that the two data points for $x < 1$ mm in figure 10(a) were not included in the calculation of the average hardness of the $Ti_{40}Zr_{15}Nb_{15}Hf_{15}Ta_{15}$ alloy.

BSE micrographs were recorded along the growth direction of the LMD specimen. Except for the presence of precipitates at $x > 23$ mm, the microstructures were similar to those of the TiZrNbHfTa alloy (figure 5) and their main features are highlighted in figure 10(a) with different colored backgrounds (e.g. yellow = dendrites, blue = chemically homogeneous single-phase bcc, and green = precipitates). The top of the compositionally graded sample ($x = 0.5$ mm) exhibits a coarse dendritic microstructure with randomly oriented dendrites enriched in Hf and Ta and interdendritic regions enriched in Ti and Zr. At $x = 3.0$ mm, the dendritic structure is still present, but the dendrites are longer, oriented vertically along the solidification direction, and their contrast is less pronounced. Below the last solidified melt pool (∼3 mm away from the top), the dendritic structure gradually disappears and completely vanishes at $x = 4$ mm (see figure 10(a)). The dendritic microstructures have been largely homogenized by solid-state interdiffusion, except for those in the last section to solidify near the top of the column. At $x > 4$ mm, the grains are elongated along the growth direction (e.g. Figures 10(b), (c)).

While the microstructures are chemically homogeneous and single-phase bcc at $4 < x < 23$ mm, precipitates are observed between 23 mm and 36 mm from the top of the specimen (region with a green background in figure 10(a)). Two locations of interest labeled *b* and *c* in figure 10(a) were imaged and the corresponding BSE micrographs are shown in figures 10(b), (c), respectively, where a remnant Vickers indent is visible in the middle of each micrograph. In figure 10(b) ($x = 24$ mm), a small fraction of the grain boundaries is decorated with precipitates. One of these is magnified in figure 10(d) where lamellar-shaped precipitates with a length of ∼4 μm grew from the grain boundary towards the left, indicating discontinuous precipitation, as discussed below. With increasing distance from the top of the compositionally

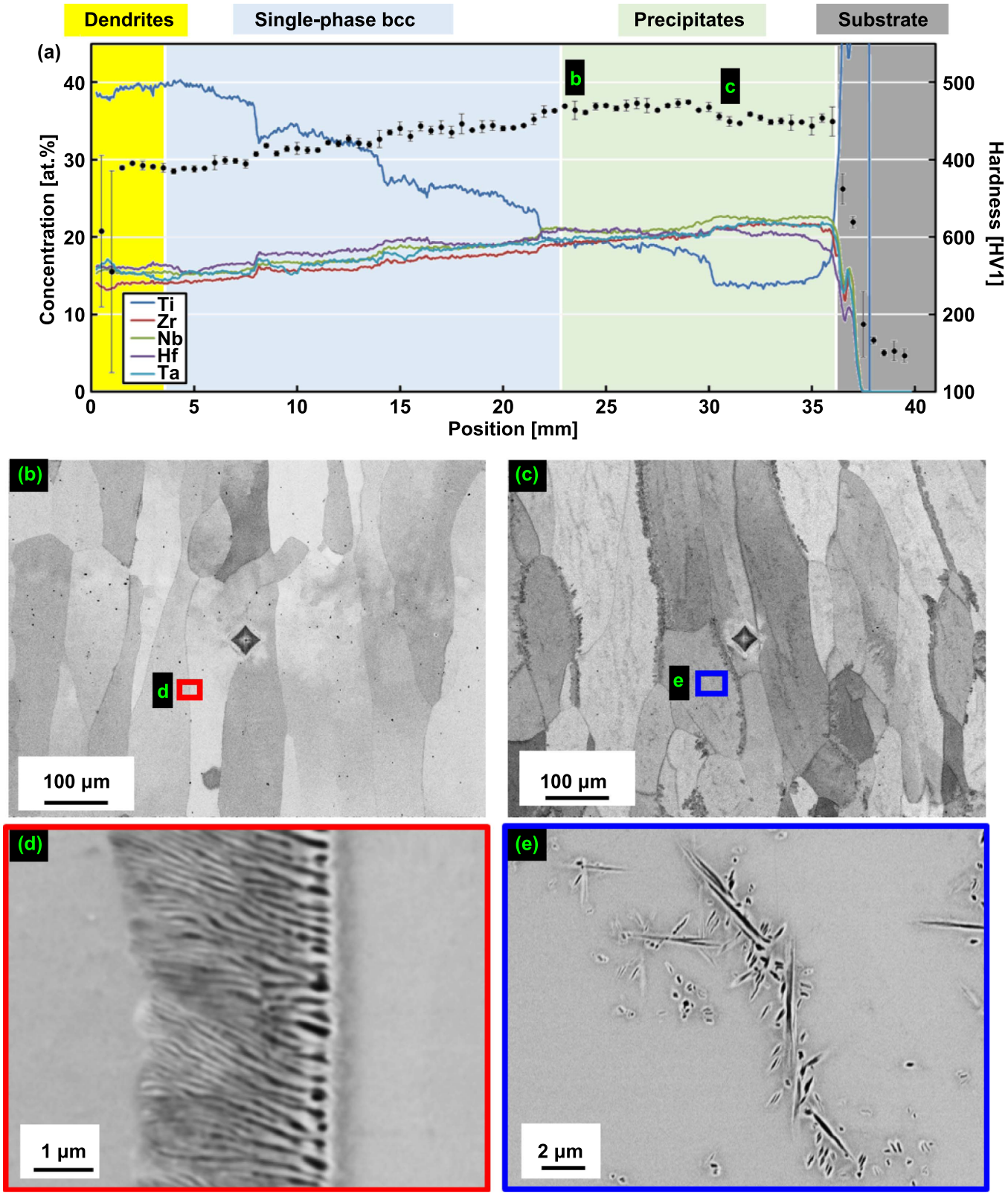

Figure 10. Compositionally graded sample built using five powder blends from the stock 1 powder. The composition was changed from $Ti_{13.3}Zr_{21.7}Nb_{21.7}Hf_{21.7}Ta_{21.7}$ (right) to $Ti_{40}Zr_{15}Nb_{15}Hf_{15}Ta_{15}$ (left). (a) The position $x = 0$ indicates the top of the columnar specimen while positions to the right of $x = 36$ mm are located within the Ti substrate. The concentrations of the alloying elements (left y-axis) are shown as continuous lines, and hardness values (right y-axis) are given with black dots and error bars. Note that the estimated O concentration increases linearly from 1.6 at.% to 2.1 at.% and the N content increases from 0.6 at.% to 0.8 at.% when x increases between 0 and 36 mm. The labels (b-c) indicate the positions where the microstructure was investigated by SEM and found to exhibit two phases. In figures (b) and (c), small areas marked with colored frames are magnified in (d) and (e), respectively. Lamellar precipitates were found at grain boundaries (b), (d) and (c), (e). Additionally plate-shaped precipitates formed within grains at location (c), (e).

graded specimen ($x > 23$ mm), both the fraction of covered grain boundaries as well as the surface area fraction of precipitates increase, figure 10(c). Additionally, needle- or plate-shaped precipitates start to appear within grains at $x > 31$ mm (see figures 10(c), (e)). The morphologies of these latter precipitates are similar to those reported by Senkov and Semiatin [7] for an equiatomic TiZrNbHfTa RHEA that was annealed at 1200 °C for 2 h and slowly cooled at a rate of 15 °C min^{-1} to room temperature. Both types of precipitates (allotriomorphs and those within grains) are darker than the matrix and are surrounded by a bright shell. EDX measurements (not shown here) were performed to identify the nature of these percipitates. The precipitates were much smaller than the electron penetration depth ($\sim$2 μm), so the EDX measurements were only qualitative. The two types of precipitates in figure 10(d), (e) were simultaneously enriched in Zr, Hf, O (the EDX peaks of O and N cannot be differentiated) and depleted in Ti and Ta. Even though these precipitates were too fine to be analyzed by EBSD, the microstructure shown in figure 10(d) strongly resembles those resulting from discontinuous precipitation, also known as cellular precipitation [55], in Ti [56] and Nb-Zr alloys [57]. Based on these studies, the dark lamellae enriched in Hf and Zr at the grain boundaries could be either bcc [56] or hcp [58] since both phases are stabilized at higher temperatures through the additions of O and N. The brighter areas between the dark lamellae in figure 10(d) are correspondingly depleted in Hf and Zr and are therefore NbTa-rich (presumably bcc). These phases are also consistent with the results of phase stability studies in the equiatomic TiZrNbHfTa RHEA [16–18]. Two different bcc phases (NbTa- and ZrHf-rich) form when the TiZrNbHfTa alloy is aged at temperatures between 800 °C and 900 °C while an additional ZrHf-rich phase with an hcp structure precipitates below 800 °C. However, further TEM work is required to determine the crystallographic structures of the precipitates.

The presence of precipitates in the compositionally graded structure for $x > 23$ mm may be rationalized as follows. During the layer-wise build-up of the LMD specimen, while the layers right below the final melt pool may be annealed in a single-phase bcc region, the temperatures within the underlying regions may fall in multi-phase regions and form precipitates. As the LMD-specimen grows, heat accumulates and the alloys near the bottom are annealed multiple times. This increases the effective annealing time and promotes precipitate formation.

Four additional compositionally graded specimens were produced from the stock 1 powder using the same processing parameters to screen the influence of individual elements on phase stability and mechanical properties. These samples were designed such that the concentration of one element varies from 13.3 to 40 at.% while retaining the other elements in equimolar proportions. The corresponding EDX concentration profiles and hardness results are shown in figure 11 for the (a) Zr-, (b) Nb- (c) Hf-, and (d) Ta-isopleths. The specimens were removed from their Ti substrates before the EDX measurements were carried out. The hardness of the 20 alloys, displayed in figure 11, will be discussed in section 4.6.

The heights, h, of the different columnar samples range between 33 mm and 41 mm. The following values reflect the average liquidus temperatures of the structures: (a) Zr-isopleth: $h = 33$ mm, $T_{liq} = 1976$ °C; (b) Nb-isopleth, $h = 40$ mm $T_{liq} = 2071$ °C; (c) Hf-isopleth, $h = 35$ mm, $T_{liq} = 2008$ °C; (d) Ta-isopleth, $h = 41$ mm, $T_{liq} = 2110$ °C. In other words, the lower the liquidus temperature, the shorter the specimen, as discussed before in section 4.3. As in figure 10(a), the Zr- and Nb-isopleths have a staircase shape, and deviations were observed for the Hf- and Ta-isopleths, figure 11. The Hf-isopleth in figure 11(c) shows a linear concentration gradient, probably due to the morphology of the Hf^{l} powder, see figure 3. The Ta-isopleth has a staircase-shaped concentration profile with enhanced scatter (figure 11(d)), probably because Ta has a very high melting point, and this compositionally graded sample contained many pores. The estimated interstitial concentrations (see section 4.4) increase linearly between the five powder blends from 1.7 at.% to 2.1 at.% for O and 0.6 at.% to 0.8 at.% for N along the Zr-, Nb-, and Ta-isopleths (from left to right in figures 11(a), (b) and (d)). The estimated interstitial concentrations decrease linearly between 3.3 at.% and 1.5 at.% for O and 1.3 at.% and 0.5 at.% for N along the Hf-isopleth (figure 11(c)). These trends reflect the fact that the Hf^{l} powder is the principal source of interstitials, i.e. the higher the Hf-concentration, the greater the interstitial content.

BSE micrographs were recorded along the height of the specimens, and the microstructures were similar to those in figures 5 and 10. To compare the different compositionally graded specimens with each other, the yellow, blue, and green backgrounds in figures 10(a) and 11 indicate the regions in which a dendritic microstructure, a chemically homogeneous bcc single-phase microstructure, or a two-phase microstructure—where precipitates form at grain boundaries and eventually within grains—were observed. The size of the region in which a dendritic microstructure was observed (yellow background in figure 11) correlates with the solidification range, ΔT: the larger the solidification range, the harder it is to homogenize the dendritic microstructure and the wider the yellow range in figure 11 ($Ti_{15}Zr_{40}Nb_{15}Hf_{15}Ta_{15}$, $\Delta T = 84$ °C; $Ti_{15}Zr_{15}Nb_{40}Hf_{15}Ta_{15}$, $\Delta T = 237$ °C; $Ti_{15}Zr_{15}Nb_{15}Hf_{40}Ta_{15}$, $\Delta T = 68$ °C; $Ti_{15}Zr_{15}Nb_{15}Hf_{15}Ta_{40}$, $\Delta T = 337$ °C).

The single-phase bcc region (blue background) is the largest for the Ti-isopleth (figure 10(a)) followed by the Zr-, Nb-, Hf-, and Ta-isopleths (figures 11(a)–(d), respectively). Several factors determine the distribution of phases. (1) The overall *alloy composition*, for obvious reasons. (2) The *interstitial content*, because it is well-known in the literature that O and N destabilize high-temperature bcc solid solutions. Since the Hf^{l} powder is the major source of interstitials, high Hf-concentrations are expected to promote precipitation indirectly. (3) The *thermal history*, i.e. *the number of thermal cycles* that an alloy undergoes and the *average thermal conductivity of the alloy* (the lower its value, the higher the annealing temperature of the underlying deposited layers). Based on this knowledge, we expect that the Hf-isopleth will have a narrow single-phase bcc region because the interstitial contents

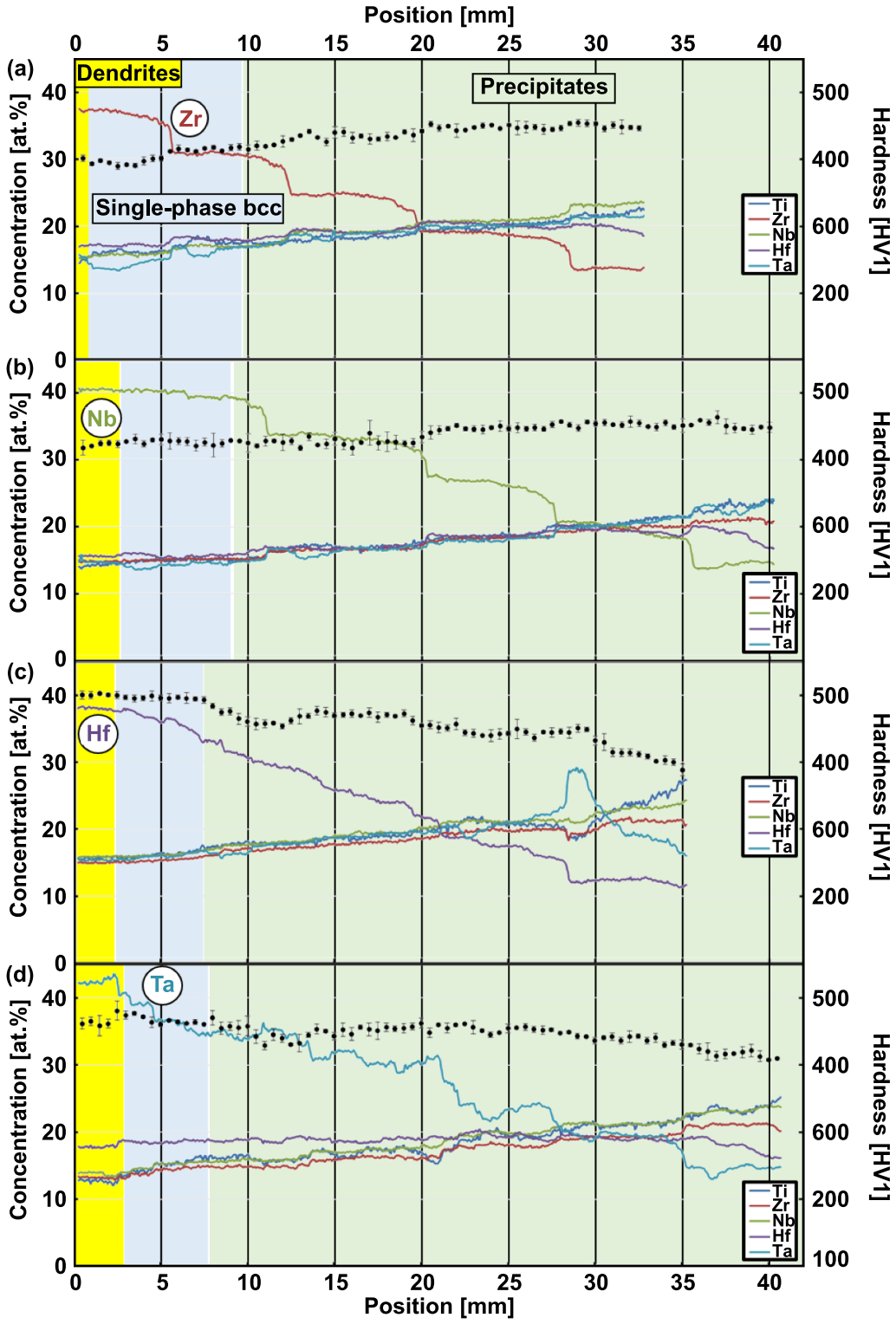

Figure 11. EDX concencentration profiles of four compositionally graded TiZrNbHfTa RHEAs produced by varying the composition of one element at a time, (a) Zr, (b) Nb, (c) Hf, and (d) Ta, from 13.3% to 40%, while retaining the other elements in equimolar proportions. Each sample was deposited using five different blends of the stock 1 powder. The position $x = 0$ indicates the top of the columnar specimen. Note that the specimens were removed from their Ti substrates before EDX measurements were performed. The concentrations of the substitutional elements are shown as continuous lines (left *y*-axis) while the corresponding hardness values are displayed as black symbols with error bars (right *y*-axis). Between the top and the bottom of each specimen, estimated interstitial contents change linearly within the following ranges: (a, b, and d) 1.7–2.1 at.% O and 0.6–0.8 at.% N and (c) 3.3–1.5 at.% O and 1.3–0.5 at.% N since the Hf[1] powder is the principal source of interstitials, see sections 3.3, 4.4 and table 1.

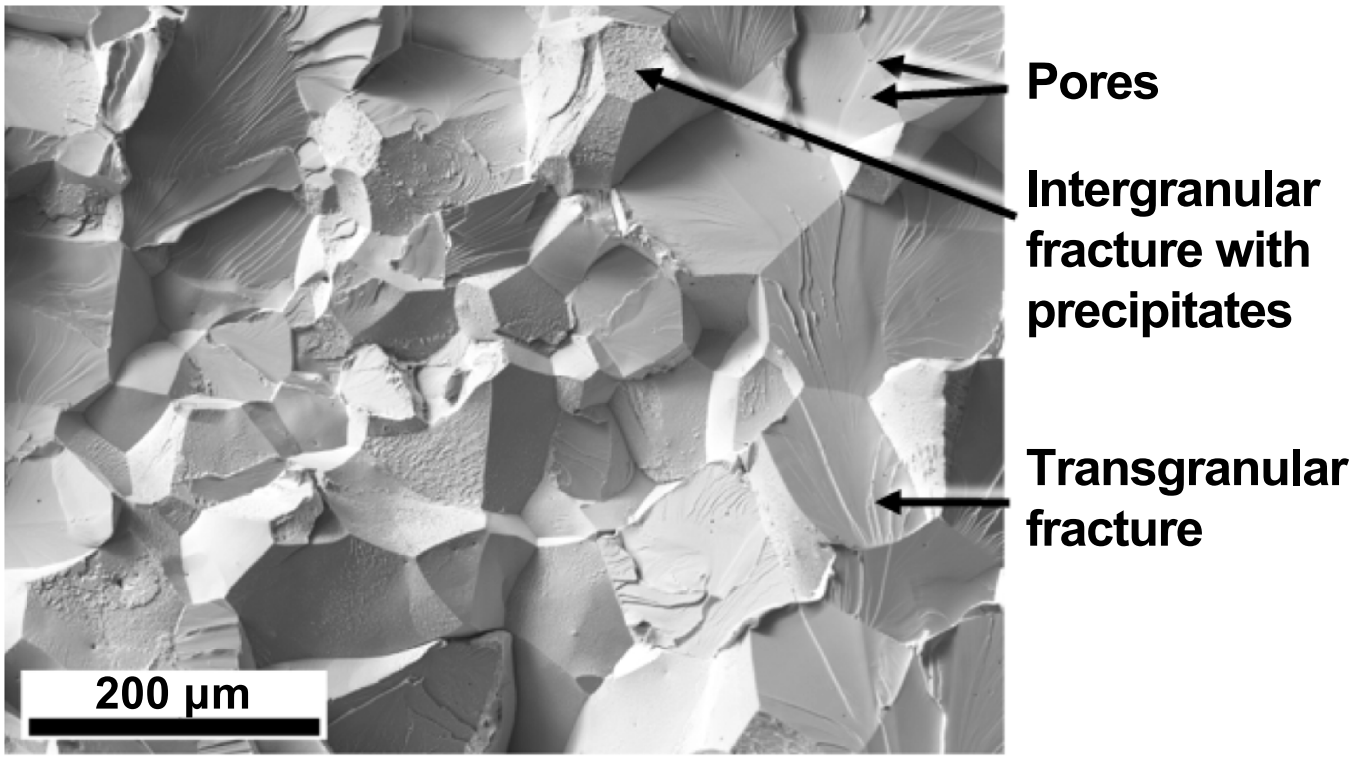

Figure 12. SEM image of a brittle fracture surface of the $TiZrNb^1Hf^1Ta^1$ alloy with a high interstitial concentration (1.89 at.% O and 0.76 at.% N). The tensile specimen broke during machining of threads in the grip section.

are high at the top of the specimen (figure 11(c)). The Nb- and Ta-isopleths are also expected to have narrow single-phase bcc regions (blue background in figures 11(b), (d)). Indeed, since the compositions in the uppermost regions have high liquidus temperatures, they contain more pores that lower the thermal conductivity of the LMD structure. As a result, the lowermost regions are annealed at higher temperatures, which may promote the formation of precipitates. In contrast, the Ti-isopleth has the largest single-phase bcc region because the liquidus temperature of the uppermost alloys is low and these alloys have low interstitial contents.

4.6. Factors affecting the strength of RHEAs

Attempts were made to machine cylindrical tensile specimens from the equiatomic $TiZrNb^1Hf^1Ta^1$ sample that was produced by LMD from the stock 1 powder with O and N contents of 1.89 at.% and 0.76 at.%, respectively. Unfortunately, the alloys fractured during the machining of the screw threads in the grip sections. One of the fracture surfaces is shown in figure 12. Both transgranular and intergranular regions are visible, and the overall fracture surface of the interstitial-rich alloy is brittle. Moreover, some of the intergranular fracture surfaces show a rough topology suggesting that grain boundary precipitates, such as those shown in figure 10(d), may have played a role in rupture. No tensile specimens could be machined out of the equiatomic $TiZrNb^2Hf^2Ta^2$ sample that was produced from the stock 2 powder since the amount of Hf^2 powder was too low to produce sufficiently 'large' tensile specimens. For these two reasons, compression specimens, which require smaller material volumes, were machined and tested to assess the mechanical behaviors of the TiZrNbHfTa RHEAs with different interstitial-contents.

A compressive engineering stress-engineering plastic strain curve at room temperature for the equiatomic $TiZrNb^1Hf^1Ta^1$ sample is shown as a black line in figure 13(a). This interstitial-rich RHEA has a very high yield stress at 0.2% plastic strain of 1460 ± 30 MPa (based on two compression tests). It work hardens until ∼12% plastic strain where the stress reaches a maximum of ∼1900 MPa. Then, cracks start growing, inducing an apparent softening of the specimen and, ultimately, failure after ∼22% plastic strain. In contrast, the interstitial-lean $TiZrNb^2Hf^2Ta^2$ RHEA that was produced from the stock 2 powder did not fracture even after 40% plastic strain (blue line in figure 13(a)). Its yield stress is 1105 ± 10 MPa, which is 25% lower than that of the interstitial-rich alloy. The $TiZrNb^2Hf^2Ta^2$ RHEA work hardens during the entire compression test. The yield stresses of $TiZrNb^1Hf^1Ta^1$ (1460 MPa) and $TiZrNb^2Hf^2Ta^2$ (1105 MPa) are both significantly greater than the compressive yield stress (930 MPa, see red line in figure 13(a)) reported by Senkov *et al* [9] for an arc-melted, hot isostatically pressed, and annealed alloy. The yield stresses of these samples also surpassed the tensile yield stress (940 MPa) given by Lilensten *et al* [59] for a recrystallized sheet. In the latter case, the O and N contents in the recrystallized sheets were later reported to be 0.27 at.% for O and 0.10 at.% for N [14]. Therefore, it appears that our samples' higher yield stresses are due to their higher interstitial contents. Differences in grain sizes can be neglected as strengthening by grain boundaries was reported

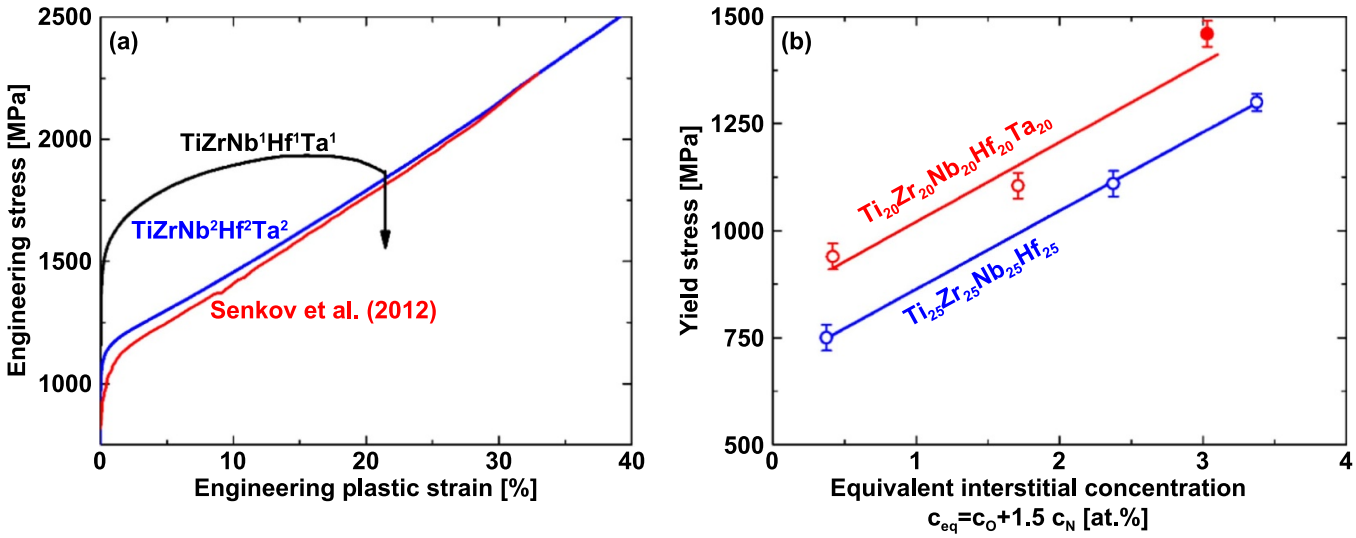

Figure 13. Effect of interstitial content on the compressive properties of equiatomic refractory alloys tested at a strain rate of 0.001 s^{-1}. (a) Stress–strain curves of interstitial-rich $TiZrNb^1Hf^1Ta^1$ RHEA (black curve) and interstitial-lean TiZrNbHfTa (blue curve), both from present study, compared to literature data for arc-melted TiZrNbHfTa (red curve) [9]. (b) Linear increase of the yield stresses of TiZrNbHfTa and TiZrNbHf alloys [22] with increasing interstitial concentration. The empty symbols are for alloys that are single-phase bcc.

to be relatively modest in this RHEA [60]. Recently, Lei *et al* [22] studied the effects of O and N additions on the strength of a quaternary TiZrNbHf RMEA. The authors showed that alloying this RMEA with 2 at.% O or 2 at.% N increased its yield stress by ∼50% and ∼75%, respectively, compared to the 'interstitial-free' alloy. N atoms are larger than O atoms, and, therefore, may distort the lattice more. Based on [22], we assumed that the effect of N on strength is 1.5 times larger than that of O and plotted yield stress as a function of an equivalent interstitial concentration defined as the sum of the O concentration +1.5 times the N concentration (figure 13(b)). Data for two alloys were plotted: the quinary TiZrNbHfTa alloy (this study and [9, 59]), and the quaternary TiZrNbHf alloy [22]. In the latter study, since the 'interstitial-free' alloy was not zone-refined and its interstitial content was not reported, we assume 'realistic' O and N contents of 0.15 at.% each. Figure 13(b) shows that the yield stresses of TiZrNbHfTa and TiZrNbHf alloys increase linearly and at the same rate with increasing interstitial concentrations. However, the quinary alloy is ∼26% stronger than the quaternary alloy over the entire range, showing the strengthening effect of adding Ta to TiZrNbHf. A possible effect of Ta is related to the fact that it increases the solidus temperature from 1776 °C for TiZrNbHf to 1849 °C for TiZrNbHfTa. Assuming both of these bcc alloys exhibit thermal and athermal regions in their yield stress versus temperature plots (similar to pure bcc metals and alloys), and the transition between the two regions occurs at the same homologous temperature, the Ta-containing quinary is expected to have a higher yield strength at room temperature than the quaternary without Ta. Based on limited experimental results [61], it is estimated that a 74 °C increase in the solidus temperature might produce a 67 MPa (9%) increase in yield strength at room temperature. Another contribution to strength is the increase in shear modulus due to Ta addition: from 25.1 GPa in TiZrNbHf [62] to 28–35.8 GPa (12%–43%) in TiZrNbHfTa [13, 14]. These individual contributions need to be isolated and carefully investigated to fully understand the reasons for the differences noted in figure 13(b).

Table 3. Vickers microhardness and compression yield stress at 0.2% plastic strain of bulk specimens. Hardness values were averaged along the sample height. Two compression specimens were machined per LMD sample. All specimens from stock 2 were tested up to a strain of 40% without fracture.

Alloy	H (HV1)	H/3 (MPa)	$\sigma_{0.2}$ (MPa)
Stock 1			
$Ti_{20}Zr_{20}Nb_{20}Hf_{20}Ta_{20}$	456	1520 ± 50	1460 ± 30
Stock 2			
$Ti_{20}Zr_{20}Nb_{20}Hf_{20}Ta_{20}$	344	1150 ± 50	1105 ± 10
$Ti_{25}Zr_{25}Nb_{25}Ta_{25}$	356	1190 ± 50	[a]
$Zr_{33.3}Nb_{33.3}Ta_{33.3}$	368	1230 ± 50	[a]
$Ti_{33.3}Zr_{33.3}Nb_{33.3}$	289	960 ± 50	795 ± 4
$Ti_{27}Zr_{27}Nb_{27}Hf_{9.5}Ta_{9.5}$	325	1080 ± 50	910 ± 50
$Ti_{42}Zr_{22}Nb_{22}Hf_7Ta_7$	275	920 ± 50	840 ± 30
$Ti_{22}Zr_{42}Nb_{22}Hf_7Ta_7$	292	970 ± 50	[b]
$Ti_{22}Zr_{22}Nb_{42}Hf_7Ta_7$	292	970 ± 50	[a]

[a]Not tested because of large pores.
[b]Not tested because of missing powder material.

The hardnesses of the various refractory alloys investigated in the present study were divided by three to obtain a rough estimate of their yield strengths. The resulting yield strengths of the refractory alloys and single-composition specimens are compared in table 3. The yield strengths estimated from the hardness values are systematically larger, by ∼10% on average, than those obtained from the compression tests. This discrepancy may be related to the following reasons. (a) Vickers hardness represents the strength at 8% plastic strain and is therefore affected by work hardening. (b) bcc alloys exhibit a large positive strain rate sensitivity of flow stress. As the strain rate during a Vickers microhardness test is

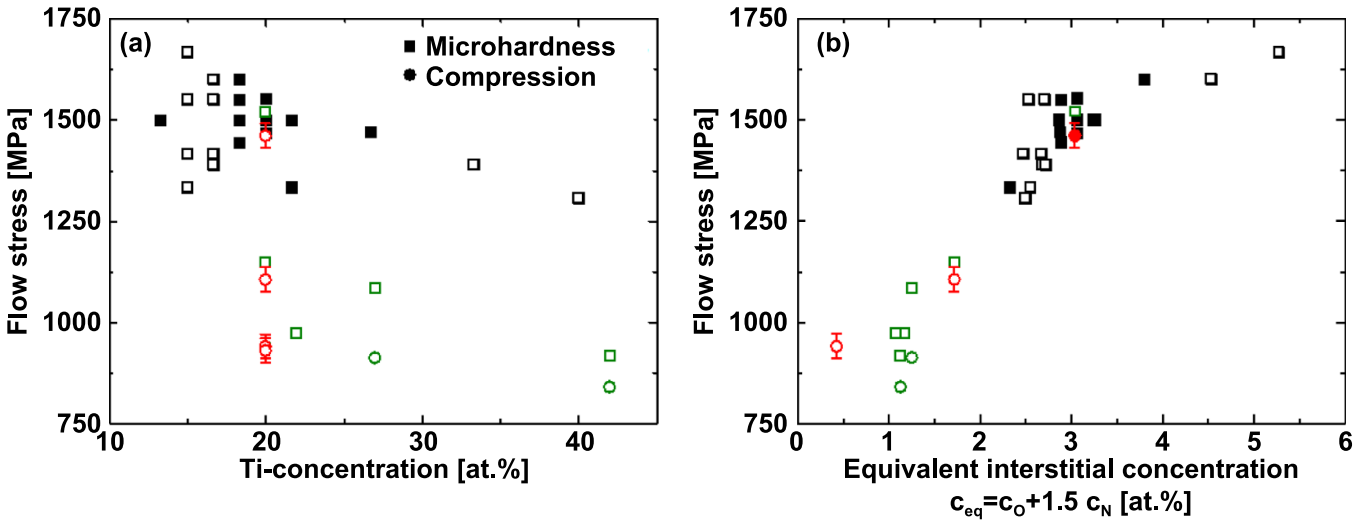

Figure 14. Effect of chemical composition on strength in refractory TiZrNbHfTa alloys. (a) Flow stress plotted versus the Ti concentration showing no clear correlation. Other plots showing the flow stress as a function of Zr, Nb, and Ta concentrations also yielded poor correlations. Much clearer relationships were obtained by plotting the yield stress either as a function of the Hf or (b) the equivalent interstitial concentration. Note that most of the interstitials originate from the Hf powders. The square- and circle-shaped data points represent flow stresses obtained with microhardness and uniaxial tests, respectively. The empty symbols mark single-phase bcc alloys. The colors of the data points highlight different data sets: chemically graded specimens (black), single-composition samples (green) and the data from figure 13(b) for the equiatomic TiZrNbHfTa alloy (red).

probably higher than that of the compression tests (0.001 s^{-1}), the flow stresses obtained from microhardness tests are expected to exceed those obtained by uniaxial tests. (c) The bulk compression specimens produced by LMD may contain small pores that result in a decrease of the apparent yield stress.

The influence of individual elements on strength of quinary TiZrNbHfTa alloys was investigated by plotting the uniaxial flow stress (circles) and the microhardness divided by three (squares) as a function of their respective concentrations in figure 14. Here, the empty symbols refer to alloys that were found to be single-phase bcc while those marked with full symbols contained secondary phases. Different data sets are represented by different colors: chemically graded and single-composition samples (black and green, respectively) and the data from figure 13(b) for the equiatomic TiZrNbHfTa alloy (red). When the flow stress is plotted as a function of the Ti concentration (figure 14(a)), the scatterplot does not show any obvious correlation and similar plots (not shown here) were also obtained for Zr, Nb, and Ta. In contrast, clearer trends with similar shapes are obtained when the flow stress is represented as a function of either the equivalent interstitial content (figure 14(b)) or the Hf concentration (not shown). Since the flow stress of a given alloy strongly increases with increasing interstitial concentration (figure 14(b)) and the interstitials mostly originate from the Hf powder (table 1), we expect that interstitials play a major role in strengthening RHEAs. Indeed, all of the data points in figure 14(b) fall within a narrow scatter band when the flow stress is displayed as a function of the equivalent interstitial concentration. For interstitial concentrations lower than 3 at.%, the flow stress increases linearly with increasing concentration at a similar rate as those shown in figure 13(b) for TiZrNbHfTa and TiZrNbHf. However, strengthening saturates at higher interstitial concentrations. Lei *et al* [22] stated that: 'Addition of more than 3.0 at.% oxygen leads to deterioration of the mechanical properties, although oxides are still not formed.' However, we did not observe a deterioration of flow stress, merely a saturation (figure 14(b)). A comparison of the data obtained for alloys containing precipitates (full symbols) and those that were found to be single-phase bcc (empty symbols) does not show any significant differences. Therefore, the strengthening due to low volume fractions of second phases can be neglected. In contrast to the flow stress, the fracture strain does deteriorate at higher interstitial concentrations (see figure 13(a)). The interstitial-rich $TiZrNb^1Hf^1Ta^1$ began breaking at a plastic strain of 12% in compression while the interstitial-lean $TiZrNb^2Hf^2Ta^2$ showed no signs of failure up to a strain of 40%.

5. Summary

LMD allows the production of equiatomic alloys and compositionally graded specimens within the Ti-Zr-Nb-Hf-Ta system. An LMD setup was developed, and columnar samples with diameters of 5–7.5 mm were deposited vertically layer by layer in an Ar atmosphere. A repetitive LMD sequence consisting of deposition and remelting steps was designed to *in-situ* alloy elemental refractory powder blends. The local melt pool produced by the laser effectively mixes the different elemental powders despite their high melting temperatures and large melting-point differences. The results obtained in the present study can be summarized as follows:

- We show that powders with irregular shapes and sizes (e.g. left of figure 4) that are usually thought to be unsuitable for LMD, because they do not flow easily, can be successfully used when a vibratory module is inserted

between the rotating disc and the storage powder container. Such a construction allows the powder blend to be fed into the melt pool.

- The dimensions of the columnar samples are affected by the liquidus temperature of the alloy for a given set of processing parameters. The melt pools of alloys with low liquidus temperatures have a low viscosity and spread laterally. As a result, these specimens have large radii and short heights. In contrast, alloys with high liquidus temperatures have smaller radii and greater heights. To maintain constant dimensions during the build, the process parameters should be adjusted both as a function of composition and as a function of build height.
- Broadly speaking, the following similarities were noted among the various alloys processed by LMD. The solidification of the final melt pool results in the formation of equiaxed dendrites with clusters of interdendritic shrinkage porosity. Alloys with high liquidus temperatures and broad solidification ranges have more severe chemical partitioning between the dendrites and the interdendritic regions. Below the melt pool, the heat introduced by the laser may homogenize the dendritic microstructures in the solid-state when the liquidus temperature and the solidification range of the alloy are not too high. However, when the height of the specimen becomes too large, the heat that accumulates during processing may trigger a phase decomposition in the lower half of the specimen. Near the substrate, the temperature of the melt pool is too low and its lifetime too short to dissolve the elemental powder particles with the highest melting points (Ta and Nb). They remain 'as is' at the bottom of the specimen.
- Pores were observed in alloys that have high melting temperatures and broad solidification ranges (e.g. TiZrNbTa, ZrNbTa). Theses pores may originate from various sources such as the evaporation of Ti, shrinkage, and interdendritic porosity, and their distribution is affected by several factors including the cooling rate of the melt pool and its viscosity.
- Two powder stocks with different interstitial contents were used to investigate their effects on phase stability and mechanical properties. Oxygen and nitrogen initially present in the elemental powders remain after LMD, which introduces ∼0.1 at.% O and ∼0.1 at.% N. The two Hf powders used in the present study were found to be the main source of interstitials.
- The upper parts of all the specimens had a bcc crystal structure since the material was annealed above its solvus temperature followed by fast cooling. In contrast, cellular ZrHf-rich precipitates formed at the grain boundaries in the lower parts of the specimens and eventually within grains. These precipitates were stabilized by the presence of interstitials and formed in regions of the specimen that were annealed multiple times during the LMD process below the solvus temperature.
- The effect on strength of individual alloying elements in TiZrNbHfTa produced by LMD is overshadowed by the interstitial strengthening; the higher the interstitial concentration, the higher the strength.

6. Outlook

Due to their high melting points and high reactivity with air, RHEAs are difficult to melt. It is even more challenging to produce structural parts with sophisticated geometries from these alloys using conventional casting methods. Arc-melting, as used in research, can produce limited quantities of RHEAs that need to be post-processed to establish suitable microstructures and machine components. Additive manufacturing is an attractive alternative due to its ability to fabricate near-net-shape parts from RHEAs or hybrid materials; for example, RHEAs could be used as coatings on components with complex geometries. RHEA coatings may be of great interest due to their superior properties at high temperatures and could provide wear and heat protection in extreme environments.

In the present study, we demonstrated the production of 1D columnar samples by LMD and highlighted key factors such as interstitial concentration, cooling rate, melting temperature, and solidification range that affect the formation of precipitates and porosity in LMD specimens that need to be taken into account and controlled when working with these alloys. For example, the precipitates that formed by discontinuous precipitation (figure 10(d)) are highly undesirable [55] as they embrittle the alloy and may reduce the lifetime of structural components during service. Based on the knowledge gained here, more research is needed in process control as well as for the production of high-purity, interstitial-free, elemental and pre-alloyed powders. This latter aspect constitutes the bottleneck for the processability and applicability of RHEAs as structural components.

Acknowledgments

GL and ELG acknowledge funding from the German Research Foundation in the framework of the priority program SPP 2006—Compositionally Complex Alloys—High Entropy Alloys, projects LA 3607/3-1 and GU 1075/12-1. EPG is supported by the U.S. Department of Energy, Office of Science, Basic Energy Sciences, Materials Sciences and Engineering Division. The center for interface-dominated, high-performance materials (Zentrum für Grenzflächendominierte Höchstleistungswerkstoffe, ZGH) is acknowledged for the use of the JEOL JSM-7200F SEM as well as the microhardness tester KB 30.

We thank Dr. J-P Couzinié from the Institute of Chemistry and Materials Paris-east, Thiais, France, for the thermodynamic calculations of liquidus and solidus temperatures. We also thank Felix Miklikowski from the chair of Applied Laser Technologies, Ruhr-University Bochum, for the production of mechanical components for the experimental LMD setup. Mike Schneider and Christian Reinhart from the chair of Materials Science and Engineering, Institute for Materials, Ruhr-University Bochum, are acknowledged for their support to perform compression tests. Finally, we thank TANIOBIS GmbH for providing the Nb and Ta elemental powders and especially Markus Weinmann for fruitful discussions.

ORCID iDs

Henrik Dobbelstein https://orcid.org/0000-0002-3809-7341
Easo P George https://orcid.org/0000-0001-9898-9694
Evgeny L Gurevich https://orcid.org/0000-0001-9451-8983
Aleksander Kostka https://orcid.org/0000-0002-8306-4709
Andreas Ostendorf https://orcid.org/0000-0002-3601-6392
Guillaume Laplanche https://orcid.org/0000-0001-9559-0928

References

[1] George E P, Raabe D and Ritchie R O 2019 High-entropy alloys *Nat. Rev. Mater.* **4** 515–34
[2] George E P, Curtin W A and Tasan C C 2020 High entropy alloys: a focused review of mechanical properties and deformation mechanisms *Acta Mater.* **188** 435–74
[3] Oses C, Toher C and Curtarolo S 2020 High-entropy ceramics *Nat. Rev. Mater.* **5** 295–309
[4] Musicó B L, Gilbert D, Ward T Z, Page K, George E P, Yan J Q, Mandrus D and Keppens V 2020 The emergent field of high entropy oxides: design, prospects, challenges, and opportunities for tailoring material properties *APL Mater.* **8** 040912
[5] Senkov O N, Wilks G B, Scott J M and Miracle D B 2011 Mechanical properties of $Nb_{25}Mo_{25}Ta_{25}W_{25}$ and $V_{20}Nb_{20}Mo_{20}Ta_{20}W_{20}$ refractory high entropy alloys *Intermetallics* **19** 698–706
[6] Senkov O N, Scott J M, Senkova S V, Miracle D B and Woodward C F 2011 Microstructure and room temperature properties of a high-entropy TaNbHfZrTi alloy *J. Alloys Compd.* **509** 6043–8
[7] Senkov O N and Semiatin S L 2015 Microstructure and properties of a refractory high-entropy alloy after cold working *J. Alloys Compd.* **649** 1110–23
[8] Couzinié J P, Dirras G, Perrière L, Chauveau T, Leroy E, Champion Y and Guillot I 2014 Microstructure of a near-equimolar refractory high-entropy alloy *Mater. Lett.* **126** 285–7
[9] Senkov O N, Scott J M, Senkova S V, Meisenkothen F, Miracle D B and Woodward C F 2012 Microstructure and elevated temperature properties of a refractory TaNbHfZrTi alloy *J. Mater. Sci.* **47** 4062–74
[10] Juan C C, Tsai M H, Tsai C W, Lin C M, Wang W R, Yang C C, Chen S K, Lin S J and Yeh J W 2015 Enhanced mechanical properties of HfMoTaTiZr and HfMoNbTaTiZr refractory high-entropy alloys *Intermetallics* **62** 76–83
[11] Juan C C, Tseng K K, Hsu W L, Tsai M H, Tsai C W, Lin C C, Chen S K, Lin S J and Yeh J W 2016 Solution strengthening of ductile refractory $HfMo_xNbTaTiZr$ high-entropy alloys *Mater. Lett.* **175** 284–7
[12] Juan C C, Tsai M H, Tsai C W, Hsu W L, Lin C M, Chen S K, Lin S J and Yeh J W 2016 Simultaneously increasing the strength and ductility of a refractory high-entropy alloy via grain refining *Mater. Lett.* **184** 200–3
[13] Dirras G, Lilensten L, Djemia P, Laurent-Brocq M, Tingaud D, Couzinié J P, Perrière L, Chauveau T and Guillot I 2016 Elastic and plastic properties of as-cast equimolar TiHfZrTaNb high-entropy alloy *Mater. Sci. Eng.* A **654** 30–38
[14] Laplanche G, Gadaud P, Perrière L, Guillot I and Couzinié J P 2019 Temperature dependence of elastic moduli in a refractory HfNbTaTiZr high-entropy alloy *J. Alloys Compd.* **799** 538–45
[15] Heidelmann M, Feuerbacher M, Ma D C and Grabowski B 2016 Structural anomaly in the high-entropy alloy ZrNbTiTaHf *Intermetallics* **68** 11–15
[16] Schuh B, Völker V, Todt J, Schell N, Perrière L, Li J, Couzinié J P and Hohenwarter A 2018 Thermodynamic instability of a nanocrystalline, single-phase TiZrNbHfTa alloy and its impact on the mechanical properties *Acta Mater.* **142** 201–12
[17] Stepanov N D, Yurchenko N Y, Zherebtsov S V, Tikhonovsky M A and Salishchev G A 2018 Aging behavior of the HfNbTaTiZr high entropy alloy *Mater. Lett.* **211** 87–90
[18] Chen S Y *et al* 2019 Phase transformations of HfNbTaTiZr high-entropy alloy at intermediate temperatures *Scr. Mater.* **158** 50–56
[19] Lilensten L, Couzinié J P, Perrière L, Bourgon J, Emery N and Guillot I 2014 New structure in refractory high-entropy alloys *Mater. Lett.* **132** 123–5
[20] Lilensten L, Couzinié J P, Bourgon J, Perrière L, Dirras G, Prima F and Guillot I 2017 Design and tensile properties of a bcc Ti-rich high-entropy alloy with transformation-induced plasticity *Mater. Res. Lett.* **5** 110–116
[21] Feuerbacher M, Heidelmann M and Thomas C 2015 Plastic deformation properties of Zr-Nb-Ti-Ta-Hf high-entropy alloys *Phil. Mag.* **95** 1221–32
[22] Lei Z F *et al* 2018 Enhanced strength and ductility in a high-entropy alloy via ordered oxygen complexes *Nature* **563** 546–52
[23] Li R D, Niu P D, Yuan T C, Cao P, Chen C and Zhou K C 2018 Selective laser melting of an equiatomic CoCrFeMnNi high-entropy alloy: processability, non-equilibrium microstructure and mechanical property *J. Alloys Compd.* **746** 125–34
[24] Zhu Z G, Nguyen Q B, Ng F L, An X H, Liao X Z, Liaw P K, Nai S M L and Wei J 2018 Hierarchical microstructure and strengthening mechanisms of a CoCrFeNiMn high entropy alloy additively manufactured by selective laser melting *Scr. Mater.* **154** 20–24
[25] Park J M, Choe J, Kim J G, Bae J W, Moon J, Yang S, Kim K T, Yu J H and Kim H S 2020 Superior tensile properties of 1%C-CoCrFeMnNi high-entropy alloy additively manufactured by selective laser melting *Mater. Res. Lett.* **8** 1–7
[26] Brif Y, Thomas M and Todd I 2015 The use of high-entropy alloys in additive manufacturing *Scr. Mater.* **99** 93–96
[27] Wu W Q, Zhou R, Wei B Q, Ni S, Liu Y and Song M 2018 Nanosized precipitates and dislocation networks reinforced

C-containing CoCrFeNi high-entropy alloy fabricated by selective laser melting *Mater. Charact.* **144** 605–10
[28] Luo S C, Gao P, Yu H C, Yang J J, Wang Z M and Zeng X Y 2019 Selective laser melting of an equiatomic AlCrCuFeNi high-entropy alloy: processability, non-equilibrium microstructure and mechanical behavior *J. Alloys Compd.* **771** 387–97
[29] Zhang H, Xu W, Xu Y J, Lu Z L and Li D C 2018 The thermal-mechanical behavior of WTaMoNb high-entropy alloy via selective laser melting (SLM): experiment and simulation *Int. J. Adv. Manuf. Technol.* **96** 461–74
[30] Qiu Z C, Yao C W, Feng K, Li Z G and Chu P K 2018 Cryogenic deformation mechanism of CrMnFeCoNi high-entropy alloy fabricated by laser additive manufacturing process *Int. J. Lightweight Mater. Manuf.* **1** 33–39
[31] Amar A *et al* 2019 Additive manufacturing of high-strength CrMnFeCoNi-based high entropy alloys with TiC addition *Intermetallics* **109** 162–6
[32] Tong Z P, Ren X D, Jiao J F, Zhou W F, Ren Y P, Ye Y X, Larson E and Gu J Y 2019 Laser additive manufacturing of FeCrCoMnNi high-entropy alloy: effect of heat treatment on microstructure, residual stress and mechanical property *J. Alloys Compd.* **785** 1144–59
[33] Gao X Y and Lu Y Z 2019 Laser 3D printing of CoCrFeMnNi high-entropy alloy *Mater. Lett.* **236** 77–80
[34] Xiang S *et al* 2019 Microstructures and mechanical properties of CrMnFeCoNi high entropy alloys fabricated using laser metal deposition technique *J. Alloys Compd.* **773** 387–92
[35] Zhang H, Pan Y and He Y Z 2011 Synthesis and characterization of FeCoNiCrCu high-entropy alloy coating by laser cladding *Mater. Des.* **32** 1910–5
[36] Huang C, Zhang Y Z, Vilar R and Shen J Y 2012 Dry sliding wear behavior of laser clad TiVCrAlSi high entropy alloy coatings on Ti–6Al–4V substrate *Mater. Des.* **41** 338–43
[37] Wu W, Jiang L, Jiang H, Pan X M, Cao Z Q, Deng D W, Wang T M and Li T J 2015 Phase evolution and properties of Al2CrFeNiMo$_x$ high-entropy alloys coatings by laser cladding *J. Therm. Spray Technol.* **24** 1333–40
[38] Zhang H, Pan Y and He Y Z 2011 Effects of annealing on the microstructure and properties of 6FeNiCoCrAlTiSi high-entropy alloy coating prepared by laser cladding *J. Therm.* Spray Technol. **20** 1049–55
[39] Ye X Y, Ma M X, Liu W J, Li L, Zhong M L, Liu Y X and Wu Q W 2011 Synthesis and characterization of high-entropy alloy Al$_X$FeCoNiCuCr by laser cladding *Adv. Mater. Sci. Eng.* **2011** 485942
[40] Joseph J, Jarvis T, Wu X H, Stanford N, Hodgson P and Fabijanic D M 2015 Comparative study of the microstructures and mechanical properties of direct laser fabricated and arc-melted Al$_x$CoCrFeNi high entropy alloys *Mater. Sci. Eng.* A **633** 184–93
[41] Chao Q, Guo T T, Jarvis T, Wu X H, Hodgson P and Fabijanic D 2017 Direct laser deposition cladding of Al$_x$CoCrFeNi high entropy alloys on a high-temperature stainless steel *Surf. Coat. Technol.* **332** 440–51
[42] Wang R, Zhang K, Davies C and Wu X 2017 Evolution of microstructure, mechanical and corrosion properties of AlCoCrFeNi high-entropy alloy prepared by direct laser fabrication *J. Alloys Compd.* **694** 971–81
[43] Ocelík V, Janssen N, Smith S N and De Hosson J T M 2016 Additive manufacturing of high-entropy alloys by laser processing *JOM* **68** 1810–8
[44] Haase C, Tang F, Wilms M B, Weisheit A and Hallstedt B 2017 Combining thermodynamic modeling and 3D printing of elemental powder blends for high-throughput investigation of high-entropy alloys—Towards rapid alloy screening and design *Mater. Sci. Eng.* A **688** 180–9
[45] Dobbelstein H, Thiele M, Gurevich E L, George E P and Ostendorf A 2016 Direct metal deposition of refractory high entropy alloy MoNbTaW *Phys. Procedia* **83** 624–33
[46] Zhang M N, Zhou X L, Yu X N and Li J H 2017 Synthesis and characterization of refractory TiZrNbWMo high-entropy alloy coating by laser cladding *Surf. Coat. Technol.* **311** 321–9
[47] Dobbelstein H, Gurevich E L, George E P, Ostendorf A and Laplanche G 2018 Laser metal deposition of a refractory TiZrNbHfTa high-entropy alloy *Addit. Manuf.* **24** 386–90
[48] Dobbelstein H, Gurevich E L, George E P, Ostendorf A and Laplanche G 2019 Laser metal deposition of compositionally graded TiZrNbTa refractory high-entropy alloys using elemental powder blends *Addit. Manuf.* **25** 252–62
[49] Li Q Y, Zhang H, Li D C, Chen Z H, Huang S, Lu Z L and Yan H Q 2019 W$_x$NbMoTa refractory high-entropy alloys fabricated by laser cladding deposition *Materials* **12** 533
[50] Moorehead M, Bertsch K, Niezgoda M, Parkin C, Elbakhshwan M, Sridharan K, Zhang C, Thoma D and Couet A 2020 High-throughput synthesis of Mo-Nb-Ta-W high-entropy alloys via additive manufacturing *Mater. Des.* **187** 108358
[51] Melia M A, Whetten S R, Puckett R, Jones M, Heiden M J, Argibay N and Kustas A B 2020 High-throughput additive manufacturing and characterization of refractory high entropy alloys *Appl. Mater. Today* **19** 100560
[52] Gibson I, Rosen D and Stucker B 2015 *Additive Manufacturing Technologies* 2nd edn (Berlin: Springer) p 258
[53] Battezzati L and Greer A L 1989 The viscosity of liquid metals and alloys *Acta Metall.* **37** 1791–802
[54] Kaptay G 2005 A unified equation for the viscosity of pure liquid metals *Int. J. Mater. Res.* **96** 24–31
[55] Porter D A and Easterling K E 1981 *Phase Transformations in Metals and Alloys* (New York: Van Nostrand Reinhold)
[56] Samimi P, Liu Y, Ghamarian I and Collins P C 2014 A novel tool to assess the influence of alloy composition on the oxidation behavior and concurrent oxygen-induced phase transformations for binary Ti–*x*Mo alloys at 650 °C *Corros. Sci.* **89** 295–306
[57] Banerjee S and Mukhopadhyay P 2007 Phase transformations, examples from titanium and zirconium alloys *Pergamon Mater. Ser.* **12** 1–813
[58] Nakai K, Kinoshita C and Kitajima S 1981 Effects of oxygen and/or nitrogen on phase transformations above the monotectoid temperature in Nb-Zr alloys *J. Nucl. Mater.* **98** 131–43
[59] Lilensten L, Couzinié J P, Perrière L, Hocini A, Keller C, Dirras G and Guillot I 2018 Study of a bcc multi-principal element alloy: tensile and simple shear properties and underlying deformation mechanisms *Acta Mater.* **142** 131–41
[60] Chen S Y, Tseng K K, Tong Y, Li W D, Tsai C W, Yeh J W and Liaw P K 2019 Grain growth and Hall-Petch relationship in a refractory HfNbTaZrTi high-entropy alloy *J. Alloys Compd.* **795** 19–26
[61] Chen S Y *et al* 2019 Peierls barrier characteristic and anomalous strain hardening provoked by dynamic-strain-aging strengthening in a body-centered-cubic high-entropy alloy *Mater. Res. Lett.* **7** 475–81
[62] Ye Y X, Musico B L, Lu Z Z, Xu L B, Lei Z F, Keppens V, Xu H X and Nieh T G 2019 Evaluating elastic properties of a body-centered cubic NbHfZrTi high-entropy alloy—A direct comparison between experiments and *ab initio* calculations *Intermetallics* **109** 167–73